Title: Metabolomic rearrangement controls the intrinsic microbial response to temperature changes

Authors: Benjamin D. Knapp[1], Lisa Willis[2], Carlos Gonzalez[3], Harsh Vashistha[4], Joanna Jammal Touma[4], Mikhail Tikhonov[5], Jeffrey Ram[6], Hanna Salman[4], Josh E. Elias[7], Kerwyn Casey Huang[1,2,7,8,†]

Affiliations:

[1]Biophysics Program, Stanford University, Stanford, CA 94305, USA

[2]Department of Bioengineering, Stanford University, Stanford, CA 94305, USA

[3]Department of Chemical and Systems Biology, Stanford University School of Medicine, Stanford, CA 94305, USA

[4]Department of Physics and Astronomy, University of Pittsburgh, Pittsburgh, PA 15260, USA

[5]Department of Physics, Washington University in St. Louis, St. Louis, MO 63130, USA

[6]Department of Physiology, Wayne State University, Detroit, MI 48201, USA

[7]Chan Zuckerberg Biohub, San Francisco, CA 94158, USA

[8]Department of Microbiology and Immunology, Stanford University School of Medicine, Stanford, CA 94305, USA

[†]To whom correspondence should be addressed: kchuang@stanford.edu

Keywords: temperature shift; Arrhenius; Michaelis-Menten kinetics; thermodynamics; entropy; enthalpy; membrane fluidity; proteomics; barcoded transposon mutant libraries; Escherichia coli; Bacillus subtilis; Schizosaccharomyces pombe; climate change

Abstract

Temperature is one of the key determinants of microbial behavior and survival, whose impact is typically studied under heat- or cold-shock conditions that elicit specific regulation to combat lethal stress. At intermediate temperatures, cellular growth rate varies according to the Arrhenius law of thermodynamics without stress responses, a behavior whose origins have not yet been elucidated. Using single-cell microscopy during temperature perturbations, we show that bacteria exhibit a highly conserved, gradual response to temperature upshifts with a time scale of ~1.5 doublings at the higher temperature, regardless of initial/final temperature or nutrient source. We find that this behavior is coupled to a temperature memory, which we rule out as being neither transcriptional, translational, nor membrane dependent. Instead, we demonstrate that an autocatalytic enzyme network incorporating temperature-sensitive Michaelis-Menten kinetics recapitulates all temperature-shift dynamics through metabolome rearrangement, which encodes a temperature memory and successfully predicts alterations in the upshift response observed under simple-sugar, low-nutrient conditions, and in fungi. This model also provides a mechanistic framework for both Arrhenius-dependent growth and the classical Monod Equation through temperature-dependent metabolite flux.

Introduction

To proliferate and survive, microbes must integrate a vast array of environmental signals such as pH[1], salt[2], osmolarity[3], and nutrient availability[4], whose effects are monitored and integrated through intracellular regulation. By contrast, while growth is critically dependent on the environmental temperature, microbes are unable to regulate intracellular temperature. Enteric bacteria face temperature changes across time scales ranging from minutes (host colonization) to hours or days (fever), and soil and marine species are regularly exposed to daily and seasonal fluctuations. The effects of temperature can be dramatic: the largest determinant of marine bacterial community composition is local sea temperature[5], and long-term temperature changes associated with climate change are thought to substantially impact soil microbial biomass[6]. Despite these fundamental connections, the mechanistic underpinnings of how temperature affects microbial behavior remain unclear.

Most studies on the cellular effects of temperature have focused on the regulatory systems that enable survival under heat and cold stress, during which molecular chaperones assist in the folding and unfolding of proteins and RNA[7,8]. While growth rate decreases at extreme, stress response-inducing temperatures[9], there is typically a temperature range over which growth rate increases with temperature in agreement with the Arrhenius Law of equilibrium thermodynamics[10,11], wherein the natural logarithm of growth rate depends approximately linearly on the inverse of the absolute temperature, with a negative slope that can be interpreted as an activation energy for growth (E_a, equivalent to the barrier for enzyme kinetics)[12]. This temperature-dependent

behavior is highly conserved across diverse bacteria, archaea, yeast, and mammalian cells[12], with each species exhibiting its own Arrhenius temperature range and activation energy.

While theoretical work has suggested that proteome stability sets the upper bound for the growth rate of a given bacterial species across temperatures[13], there is no correlation between permissible (optimal) growth temperatures and E_a across bacteria[10], indicating that E_a is likely influenced by factors other than proteome stability. In *Escherichia coli*, the Arrhenius range is between 23 °C and 37 °C and E_a is ~13 kcal/mol[11,13], similar to the free energy change from ATP hydrolysis (12–16 kcal/mol)[14], suggesting that there may be a single rate-limiting enzyme for growth. On the other hand, theoretical work on cyclical enzyme networks has suggested that E_a arises from the average of the activation energies over all reactions within the network[15,16], as the E_a for most biological enzymes is constrained between 5–20 kcal/mol[12,17,18]. However, the factor(s) that limits growth across Arrhenius temperatures and sets E_a for a given species remains unknown.

Most previous studies of growth in the Arrhenius range have focused on steady-state growth, rather than how cells respond to temperature changes. An early study of 133 proteins in *E. coli* showed that the concentration of most of these proteins was maintained across Arrhenius temperatures, suggesting that the proteome may be largely temperature insensitive[11]. However, other studies found transient changes in the synthesis of tRNA synthetases after temperature increases[19], and a decrease from

37 °C to 28 °C resulted in significant changes to ~9% of the *E. coli* transcriptome[20], perhaps reflecting the selection for coupled sensing of changes in temperature and other environmental variables such as oxygen levels relevant for animal host colonization[21]. In the few studies examining the growth rate response to temperature shifts, some report that *E. coli* growth rate responds almost immediately upon temperature shifts within the Arrhenius range[19,22], while others report much longer time scales that scale with the final temperature[23].

Many factors could determine the time scale of temperature adaptation. *E. coli* cells tightly maintain membrane fluidity across all temperatures permissible for growth by regulating membrane composition[24]. Increased membrane fluidity allows for higher respiratory metabolic rates[25], but how fluidity impacts growth rate during temperature shifts is unknown. Growth rate across nutrients correlates with ribosome concentration, which is optimized through competition between protein and autocatalytic ribosome synthesis[26,27]. As a result, many models of growth focus on translation as a key growth-limiting factor[28]. However, this framework is likely inappropriate for understanding growth rate variations across temperatures, as ribosome concentration is constant across Arrhenius temperatures[11,29].

Here, we demonstrate that *E. coli* cells exhibit an asymmetric growth-rate response to temperature shifts within the Arrhenius range: during downshifts, growth-rate rapidly decreases on the same time scale as that of the temperature shift, while cells gradually adapt to upshifts on a time scale corresponding to ~1.5 doublings at the steady-state

growth rate of the final temperature, independent of nutrient source. We show that these responses do not result from proteome or membrane reconfiguration or from transcriptional regulation, although increased membrane fluidity was lethal at high temperatures. To interrogate the mechanism underlying growth-rate adaptation to temperature shifts, we developed an autocatalytic enzyme network model that incorporates temperature-sensitive Michaelis-Menten kinetics into chained reactions. The model quantitatively captured the asymmetric responses to up- and downshifts across Arrhenius temperatures and how carbon source affects the dynamics immediately after an upshift through changes in the activation energy of growth. Furthermore, our model successfully predicted the larger initial acceleration and decrease in upshift response time observed at sub-saturating substrate concentration compared with saturation. Growth-rate dynamics during temperature upshifts were highly conserved across diverse *Escherichia* strains/species and the Gram-positive *Bacillus subtilis*, suggesting that certain aspects of microbial responses to temperature shifts and hence features of the underlying metabolic network may be universally conserved. Moreover, the ability of the model to capture the distinct response of the fission yeast *Schizosaccharomyces pombe* suggests that temperature adaptation provides a window into the factors limiting growth.

Results

The response time to temperature upshifts is determined by the steady-state growth rate at the higher temperature

To determine whether evolutionary history impacts temperature sensitivity across strains of a single species, we measured the growth of 12 *E. coli* strains isolated from fecal samples of hosts encompassing a broad range of body temperatures (Table S1)[30,31]. All strains exhibited similar temperature sensitivity profiles, with Arrhenius behavior (linear relationship between ln(growth rate) and 1/*T*) between 27 °C and 37 °C (Fig. S1B), with similar activation energies (10–15 kcal/mol) of growth (Fig. S1C–E), consistent with a null model in which growth is determined by a single rate-limiting enzyme. Single-cell growth rates were highly correlated with bulk growth rates from liquid culture across the Arrhenius range (Fig. 1A, inset, S2). These data suggest that the thermodynamic properties of *E. coli* growth are conserved and that host body temperature does not dictate the temperature sensitivity of enteric bacteria.

To identify the mechanisms underlying the temperature sensitivity of bacterial growth, we used single-cell tracking with a microscopy-compatible temperature controller[32] to interrogate hypotheses about the molecular architecture underlying temperature sensitivity. For the null model in which growth depends only on a single rate-limiting enzyme, instantaneous growth rate (defined as $\frac{1}{L}\frac{dL}{dt}$, Methods) would adapt immediately to the steady-state value dictated by the current temperature. Hence, the time scale of growth-rate adaptation would match that of a temperature shift. To test whether such a

153 minimal model applies to *E. coli*, we monitored the growth of single cells on LB agarose
154 pads during 10 °C temperature shifts within the Arrhenius range (between 27 °C and
155 37 °C). A rapid downshift from 37 °C to 27 °C resulted in a rapid decrease in growth rate
156 with a time scale quantitatively similar to that of temperature (Fig. 1B, S3), nearly
157 reaching the steady-state growth rate at 27 °C, and then slowly decelerating toward the
158 new steady state (Fig. 1B).
159
160 By contrast, temperature upshifts from 27 °C to 37 °C resulted in a slow and
161 qualitatively distinct response from downshifts, with an initial "spike" that peaked at ~3
162 min post-shift and subsequent linear acceleration until reaching the 37 °C steady-state
163 growth rate at ~40 min post-shift (Fig. 1C), a response time (Methods) substantially
164 longer than the doubling time at 37 °C (~22 min). To identify factors that affect the
165 response time to temperature upshifts, we shifted *E. coli* from steady-state growth on
166 LB at 27 °C to 30 °C, 33 °C, or 37 °C. In each case, the upshift caused an initial spike
167 and subsequent linear acceleration up to the steady-state growth rate at 37 °C (Fig.
168 1C,D). However, the time scale of the overall response depended on the final
169 temperature. When cells were shifted to 33 °C, the response time was longer than after
170 an upshift to 37 °C, despite the smaller difference in steady-state growth rate between
171 the initial and final temperature, and the response time for the shift to 30 °C was even
172 longer (~60 min, Fig. 1D).
173
174 To test whether the response is largely determined by the increased growth rate at the
175 elevated final temperature, we normalized time t by the doubling time at the final

176 temperature (τ_D) to obtain the thermal time t/τ_D (Fig. 1E). After normalizing the change
177 in growth rate by the difference in steady-state growth rate at the initial and final
178 temperature, all trajectories collapsed onto a single curve, with response time of 1.6±0.2
179 doublings at the final temperature (Fig. 1F, Methods). Similar collapse was observed for
180 a broad range of temperature upshifts (Fig. 1F), including to temperatures outside the
181 Arrhenius range (Fig. S4), and across growth media (Fig. 1G,H), suggesting a highly
182 conserved behavior.
183
184 Temperature upshift responses were largely unaffected by the presence of oxygen (Fig.
185 S5A,B) or chaperones (Fig. S5C-E). Under nutrient limitation, the enzymes SpoT and
186 RelA produce the alarmone ppGpp, which signals large-scale transcriptional
187 reprogramming known as the stringent response that regulates metabolism[33,34]. During
188 an upshift from 27 °C to 37 °C, the response time of a Δ*spoT* Δ*relA* mutant was longer
189 than the parent strain's (Fig. S5G), and an upshift from 27 °C to 42 °C caused Δ*spoT*
190 Δ*relA* cells to rapidly decelerate from 0.8 h^{-1} to 0.4 h^{-1} (Fig. S5H), consistent with the
191 transient increase in ppGpp previously observed in these conditions[19,35]. Thus, the
192 stringent response is important for growth at heat-shock temperatures, and its impact on
193 the growth response to upshifts suggests that the response time scale is related to
194 metabolism.
195
196 **Downshift pulses reveal a temperature memory**
197 Since adaptation to an upshift requires longer than the doubling time at the final
198 temperature, it is likely that a component(s) limiting for growth must be produced to

199 attain the steady-state growth rate at the higher temperature. In the absence of rapid
200 degradation, after a temperature downshift the level of such a limiting component would
201 represent memory of the growth state at the higher temperature until it is slowly diluted
202 by growth down to its steady-state value at the lower temperature. To evaluate this
203 hypothesis, we monitored MG1655 cells during temperature downshift pulses from
204 37 °C to 25 °C and back to 37 °C of varying duration. As we hypothesized, after a short
205 (10 min) interval at 25 °C, instantaneous growth rate quickly (within <10 min) recovered
206 back to the 37 °C steady state (Fig. 1I, S6A), accompanied by a larger spike than for
207 cells starting from steady-state growth at 25 °C (Fig. 1I, S6A). For the longest interval at
208 25 °C (30 min), the response time after the upshift back to 37 °C was still faster (~25
209 min, Fig. 1I, S6A) than the steady-state response (~40 min), indicating that cells did not
210 fully equilibrate to 25 °C 30 min after a downshift from 37 °C. Furthermore, cells shifted
211 back to an intermediate temperature (30°C rather than 37 °C) after 5 min at 23 °C were
212 able to reach the new steady-state growth rate almost immediately (Fig. S6B). Short
213 pulses (5–10 min) at extreme temperatures (<20 °C or >42 °C) from 37 °C generally
214 induced rapid deceleration (Fig. S7), but cells rapidly exited these pulses with large
215 spike responses and re-achieved steady-state growth at 37 °C within 10–20 min (Fig.
216 S7B,C,E). These results suggest that a growth-limiting component is slowly diluted at
217 the lower temperature, as cells can respond quickly to (even extreme) temperature
218 fluctuations.
219

220 **The *E. coli* proteome is mostly invariant across temperatures in the Arrhenius**
221 **range**

222 The prevailing model for growth optimization across nutrient conditions is that growth
223 rate and ribosome concentration are directly coupled[28,36,37], due to the limitation that
224 ribosomes must produce themselves in addition to all other proteins[26,38]. Within this
225 picture, the rapid response to temperature downshifts and the history dependence of
226 growth rate during downshift pulses might be due to proteins limiting for growth at
227 higher temperatures being overly abundant during the downshift, while the slow
228 response to upshift would be due to the need for proteome reallocation[39].
229
230 To test this hypothesis, we performed untargeted proteomics (LC-MS/MS, Methods) on
231 *E. coli* MG1655 during steady-state growth on three media (LB or minimal media
232 supplemented with glucose or glycerol) at 25 °C, 30 °C, and 37 °C. Of the 4,285 known
233 open reading frames in the *E. coli* MG1655 genome, 1,918 (44.8%) proteins were
234 identified across all samples and biological replicates, similar to the proteome recovery
235 rate of previous studies[40], accounting for ~91% of the total proteome estimated from
236 ribosomal profiling (Fig. S8A)[41] with high replicability (r=0.96–1.0) (Fig. S8B,C). We
237 annotated each protein utilizing a modification of the Clusters of Orthologous Groups
238 (COG) database[42] (Fig. 2A; Methods). As expected, at 37 °C the ribosomal protein
239 fraction was positively correlated with the growth rate in each medium (Fig. 2B, light
240 blue), while energy and metabolism fractions were negatively correlated with growth
241 rate (Fig. 2C, light blue). However, the fraction associated with each functional group
242 was virtually constant across Arrhenius temperatures in each medium (Fig. 2D,E,
243 S8D,E). We only observed significant changes for temperatures outside the Arrhenius
244 range (16 °C, 43 °C) that were consistent with known stress-response pathways (Fig.

245 S8D,F,G)[13]. Thus, ribosome fraction is unlikely to drive growth rate changes across
246 temperatures.
247
248 Most individual protein fractions were constant across temperatures; only 13 proteins
249 exhibited a >2-fold change between 25 °C and 37 °C independent of growth medium
250 (Fig. S9). The most temperature-dependent protein was the DNA-binding StpA[43], which
251 increased ~14-fold between 25 °C and 37 °C (Fig. S9A). Nonetheless, Δ*stpA* cells
252 exhibited a similar response to an upshift from 25 °C to 37 °C on LB as wild-type cells
253 (Fig. 2F,G), as did individual knockouts of the three next most temperature-dependent
254 proteins (Fig. 2F,G, S9). Thus, the *E. coli* proteome is largely insensitive to temperature
255 at steady state, and proteins with the largest abundance changes across Arrhenius
256 temperatures do not impact the growth-rate response to temperature upshifts.
257
258 **Functional genetic screening did not identify any genes associated with**
259 **temperature upshifts**
260 While proteomics did not identify large-scale rearrangement between temperatures at
261 steady state (Fig. 2), we interrogated whether some genes determine the non-steady-
262 state dynamics between temperatures (Fig. 1B,C). To test this possibility, we performed
263 a genome-wide, time-resolved screen using a pooled, randomly barcoded transposon
264 mutant library in *E. coli* BW25113[44], whereby the relative abundance of each mutant
265 was quantified in high throughput during temperature shifts between 25 °C and 37 °C
266 (Fig. 3A, S10A–C,F,G) (Methods). No gene disruptions were consistently identified
267 across biological replicates with a significant fitness defect specific to the temperature

268 upshift (Fig. 3B,C, S10C–E). The only gene of significance from our screen was *uup*
269 (Fig. 3D, S10G), which encodes an ABC-F protein[45]. Δ*uup* cells exhibited slight growth
270 defects at both 27 °C and 37 °C (Fig. 3E), in contrast to other ABC-F mutants (Fig.
271 S10H,I), and the response time after a temperature upshift was substantially longer
272 (~2.7 doublings versus ~1.6 for wild type) (Fig. 3F), likely due to defects in ribosome
273 assembly[46]. Taken together, this screen suggests that none of the nonessential genes
274 are responsible for the delayed growth-rate response to temperature upshifts.
275
276 To investigate the role of essential genes during temperature upshifts, we treated *E. coli*
277 cells with a variety of antibiotics at sub-minimum inhibitory concentration (MIC) levels[47]
278 and subjected them to temperature upshifts from 27 °C to 37 °C on LB (Fig. S11).
279 Response times remained ~1.5 doublings for treatment with antibiotics that target the
280 ribosome (Fig. 3G,H, S11A,B), DNA replication, and transcription, despite large impacts
281 on growth rate in some cases (Fig. S11C,D). Only at high concentrations of fusidic acid
282 (50 μg/mL), which disrupts translational translocation and ribosome disassembly[48], did
283 we observe a significant decrease in response times (~0.2 doublings; Fig. S11F,G). We
284 observed similar effects in knockouts of genes responsible for tRNA modification (*tusA*,
285 *tusB*)[49] (Fig S11F,G), suggesting that severely impaired translational capacity under
286 high amino acid availability causes a mismatch, allowing for fast response times.
287
288 Membrane fluidity is exquisitely regulated in *E. coli* across temperatures: the fraction of
289 unsaturated fatty acids decreases with increasing temperature to maintain viscosity[24,25].
290 Triclosan, which targets membrane synthesis, increased the response time to ~2.5

291 doublings (Fig. 3G,H), suggesting that the delay in growth rate might be due to the need
292 to alter membrane composition. However, disruptions to the regulation of *fabB*, which
293 encodes the major β-ketoacyl-[acyl carrier protein] synthase responsible for elongating
294 unsaturated fatty acids[50,51], had little effect on upshift response times, despite significant
295 changes to membrane fluidity (Fig. 4A–D) (Methods). While an increase in membrane
296 fluidity conferred a growth advantage at 37 °C (Fig. 4F), we found that increases in
297 membrane fluidity negatively affected cell growth and survival at temperatures >42 °C
298 (Fig. 4G,H). Thus, while membrane fluidity does not determine the time scale of upshift
299 responses, its regulation is critical for cell integrity at high temperatures.
300

301 **A temperature-sensitive enzyme network (TSEN) model captures temperature-**
302 **shift response dynamics**

303 Our findings indicate that the normalized response time to temperature upshifts is
304 largely conserved (Fig. 1F,H, 2G, 3H, 4E, S5B,E, S10I, S11B,D). Our proteomic,
305 genetic, and chemical screens largely failed to uncover a key molecular regulator of the
306 response, leaving it unclear how the response behavior arises and what factors set the
307 time scale. To interrogate the mechanisms underlying these phenomena, we developed
308 an autocatalytic network model of growth, since such models have a long history in
309 enzyme kinetics[15].
310

311 To model growth, we incorporated three general classes of reactions: (1) import, (2)
312 metabolite production, and (3) volume expansion (Fig. 5A). Each reaction obeys

Michaelis-Menten kinetics, such that metabolite c_i is consumed by enzyme e_i to produce the next metabolite c_{i+1} in the network:

$$c_i + e_i \rightleftharpoons (c_i e_i)^* \longrightarrow c_{i+1} + e_i. \quad (1)$$

In a linear network (no branching), the dynamics of each intermediate metabolite are dictated by

$$\frac{dc_i}{dt} = \frac{k_{i-1} e_{i-1} c_{i-1}}{K_{i-1} + c_{i-1}} - \frac{k_i e_i c_i}{K_i + c_i} - c_i g, \quad (2)$$

where the first two terms on the right-hand side reflect enzymatic production and consumption of c_i and the last term accounts for dilution via growth at the rate g (SI). e_i is the concentration of the ith enzyme, k_i is its catalytic rate, and K_i is its Michaelis-Menten constant. Importantly, we consider the possibility that both k_i and K_i are temperature dependent with Arrhenius behavior (Fig. 5A, SI), consistent with experimental measurements of several enzymes[52-54]. After the final step of a reaction network of size *N*, an enzyme e_N consumes c_N to expand cell volume at a rate $g = \gamma_0 \frac{k_N e_N c_N}{K_N + c_N}$, where γ_0 is an efficiency factor assumed to be constant in a given environment, reflecting the conversion of c_N to a structural component of the cell envelope (SI). From physical considerations of glucose uptake and growth rate constraints (SI), we estimated that γ_0 is ~0.03 mM^{-1}. We call these equations a temperature-sensitive enzyme network (TSEN) model.

Since the proteome is largely maintained across temperatures (Fig. 2E, S8D), we assumed that the concentration of each enzyme remains constant during any temperature shift. In a simple version of our model with two intermediate metabolites

335 (minimal TSEN), we considered a single intermediate reaction between import and
336 growth and set each kinetic parameter to be identical across reactions (Fig. 5A). We
337 also assumed a high (saturating) concentration of the external substrate. At a given
338 temperature, the system reaches a steady state with stable concentrations of the
339 intermediate metabolite.
340
341 We simulated the model to reach a steady state at 27 °C and then shifted the
342 temperature to 37 °C. The system exhibited a non-zero response time to reach the
343 steady-state growth rate at 37 °C (Fig. 5B). To increase growth rate by 95% of the
344 difference between 27 °C and 37 °C required ~2 doublings (Fig. 5B), similar to our
345 experimental observations (Fig. 1F,H). Variations in kinetic parameters largely
346 maintained response times of 1–2 doublings (Fig. S12A,B), as long as the E_a for the
347 catalytic rate of the import reaction was above that of the other catalytic rates
348 (production, growth) (Fig. S12B). However, if the activation energy for all Michaelis-
349 Menten constants is 0, then the growth rate response is also immediate (Fig. 5B),
350 highlighting the importance of temperature sensitivity of K_i. Furthermore, the version of
351 the minimal TSEN without an intermediate reaction ("production-less" TSEN, SI) is
352 analytically tractable and predicts an upshift response time between 1.1 and 2.3
353 doublings for a growth-rate cut-off between 95% and 99% of the difference between
354 steady-state growth rates (Fig. S12C–F), in agreement with our measurements (~1.5
355 doublings, Fig. 1F,H), suggesting that the precise definition of the response time scale
356 is not critical for producing physiological timescales. Additionally, the minimal TSEN

357 produces an Arrhenius-like growth rate (Fig. S12G), in agreement with observations[10,12]
358 (Fig. 1A, S1, S2).
359
360 For a reaction network with *N* intermediates, the analytical solution of steady-state
361 growth rate (SI) is

362 $$g = \frac{\frac{k_0 e_0 c_0}{K_0 + c_0}}{\frac{1}{\gamma_0} + \sum_{i=1}^{N} c_i}, \quad (3)$$

363 which is set by the import rate $\frac{k_0 e_0 c_0}{K_0 + c_0}$, growth efficiency factor γ_0, and the total
364 intracellular metabolite concentration $\sum_{i=1}^{N} c_i$. Since import changes instantaneously with
365 temperature, the response time scale is associated with rearrangement of the
366 metabolome. Eq. 3 also reflects that growth comes at the cost of storing metabolic
367 intermediates c_i, and holds regardless of branching within the network (SI). This model
368 recovers the well-known Monod Equation as long as import follows Michaelis-Menten
369 kinetics[55] (SI), which has been shown for a variety of sugar transporters in *E.* coli[56-58].
370
371 In *E. coli*, the majority of major metabolites are present at concentrations that saturate
372 their respective enzymes[59]. However, many central-carbon reactions operate near their
373 K_M[59], suggesting that bottlenecks are highly likely. Moreover, enzymes that catalyze
374 product formation tend to have higher activation energy than transporters[60]. Within a
375 simple network involving import, production, and growth, introducing a bottleneck into
376 the production reaction characterized by a large and temperature-sensitive K_M
377 ($K_M(T = 37\ ^\circ\mathrm{C}) = 20\ \mathrm{mM}$, E_a=22.5 kcal/mol) produced strikingly physiological behavior:
378 simulations predicted an initial spike similar to our experimental observations and a

379 response time of ~2 doublings (Fig. 5B). Moreover, when the bottleneck was within a
380 pathway involving multiple production reactions, the spike broadened, and the
381 acceleration dynamics were quantitatively similar to our experimental measurements
382 (Fig. 5C). This TSEN model readily predicts asymmetric behavior between upshifts and
383 downshifts (Fig. 5D); such asymmetry is expected from temperature-dependent
384 Michaelis-Menten kinetics[12]. Additionally, after the initial large decrease in growth rate
385 upon a downshift, the multiple-reaction model predicts a slow deceleration toward the
386 slower steady-state growth rate (Fig. 5D, dark blue), similar to our experimental
387 observations (Fig. 1C, S2). Thus, an initial spike, a physiological response time, and
388 asymmetric behavior emerge from only a few simple assumptions about the network.
389

390 **Spike and response time are dictated by metabolome rearrangement**

391 In the bottlenecked TSEN model, metabolites after the bottleneck undergo a transient
392 decrease in concentration after a temperature upshift (Fig. 5E) that agrees with the time
393 scale of the spike response (Fig. 5D), suggesting that spikes are caused by rapid
394 consumption of post-bottleneck metabolites. Meanwhile, metabolites before the
395 bottleneck gradually build up, as do the post-bottleneck metabolites after the spike, until
396 metabolome rearrangement has stabilized (Fig. 5E). As a result, final growth rate (which
397 scales with temperature) dictates the thermally limited response time necessary to
398 rearrange the metabolome. Simulations of our model captured the near invariance of
399 the normalized response time across initial and final temperatures (Fig. 5F) as
400 represented by linear scaling of absolute response time with doubling time at the higher
401 temperature (Fig. 5G). This scaling was consistent with our experimental measurements

402 (Fig. 2E), which exhibited a slope of 1.4±0.3 (Fig. 5H), consistent with the range of
403 normalized response times measured across temperatures and growth media (Fig.
404 1F,H).
405
406 **TSEN model predicts spike dependence on nutrient type**
407 Early work by Monod and others demonstrated that *E. coli* growth rate depends on
408 glucose concentration in a manner remarkably similar to Michaelis-Menten enzyme
409 kinetics with a half-saturation constant K_M~22 μM[55]. This relationship is referred to as
410 the Monod Equation,

411 $$g = \frac{g_{\max} c}{K_M + c}, \tag{4}$$

412 where c is the concentration of the substrate (e.g., glucose) and $g_{\max}$ is the growth rate
413 when $c \gg K_M$. This equation is highly similar to the steady-state growth prediction from
414 the TSEN model (Eq. 3), which predicts that $g_{\max}$ and K_M are largely determined by
415 import, which in turn likely depends on the specific substrate. To examine how these
416 temperature-dependent parameters vary with growth substrate, we measured the
417 growth rate $g_{\max}$ and K_M at various temperatures across a variety of media, including
418 simple sugars, casamino acids, and rich medium (LB) (Fig. S13A–C; Methods). Our
419 measurements showed that growth on simple sugars produces Monod-like behavior
420 with large E_a for $g_{\max}$ (12–25 kcal/mol) and small, temperature-insensitive K_M (0.04–0.3
421 mM) (Fig. S13C–F). Conversely, amino acid growth was characterized by smaller,
422 concentration-dependent E_a for $g_{\max}$ (3–15 kcal/mol) with large, temperature-sensitive
423 K_M (1–9 mM) (Fig. S13C–G).
424

425 Despite the higher temperature sensitivity (E_a) of steady-state growth rate in glucose
426 compared with casamino acids or LB (Fig. S13), the normalized response time for an
427 upshift was highly similar across these nutrients (Fig. 1H), as predicted by our TSEN
428 model, wherein increases in the activation energy of the import reaction have little effect
429 on response times (Fig. S12B). However, the spike was much smaller or nonexistent in
430 glucose (Fig. 1H). Motivated by this decoupling of response time and spike height, we
431 probed the behavior of our TSEN model when changing the activation energy of the
432 catalytic rate of the import reaction to mimic the differences between LB and glucose.
433 The TSEN model predicts that spike height should decrease sharply when the activation
434 energy of import is >15 kcal/mol (Fig. 6A), while the response time increases by only
435 ~0.1 doubling (Fig. 6B). Thus, the model predicts that activation energy differences
436 between nutrient types (Fig. S13F,G) are sufficient to explain differences in the initial
437 spike behavior observed across growth media (Fig. 2G,H).
438

439 **TSEN model predicts a metabolically encoded temperature memory**

440 While growth rate rapidly decreases after a downshift in our model (Fig. 5D), the
441 concentration of metabolites requires dilution to equilibrate, which takes place on the
442 time scale of growth. Thus, during a transient downshift pulse, the cell gradually
443 transitions from the high temperature to the low temperature metabolic state, despite
444 rapid growth deceleration. Indeed, simulations of the bottle-necked TSEN model (Fig.
445 5C) during a downshift pulse from 37 °C to 27 °C back to 37 °C, with variable duration
446 at 27 °C, resulted in faster upshift responses than from the steady state at 27 °C (Fig.
447 6C). More than a doubling at 27 °C was required for recovery of the upshift response

time (Fig. 6D) and the spike height remained higher than for an upshift from steady state for pulses of multiple doublings (Fig. 6E), again collectively consistent with our experimental data (Fig. 1I, S7). These findings highlight the ability of our model to reproduce nearly all observed temperature-shift responses with reasonable quantitative agreement, underscoring the importance of the temperature sensitivity of import and metabolome rearrangement in upshift responses.

TSEN model successfully predicts temperature upshift response at low substrate concentration

Although we have thus far focused on experimental conditions in which the external substrate concentration is saturating, nutrient concentrations are low in many environments. Since a key feature of the ability of our model to successfully predict upshift responses is the temperature sensitivity of Michaelis-Menten constants, we were motivated to examine the low-nutrient regime. To examine this regime, we simulated our model with external concentrations below the K_M for import and considered a temperature upshift from 27 °C to 37 °C. At $c_0 < K_0$, the relative spike height increased substantially, and the normalized response time decreased with decreasing concentration (Fig. 6F–J). This decrease in response time occurred because the increase in import rate after a temperature upshift is smaller when $c_0 \leq K_0$ compared with $c_0 \geq K_0$[12], despite an identical increase in catalytic rates that consume the imported metabolite. The activation energy for growth was also predicted to decrease with decreasing nutrient concentration (Fig. 6H), in agreement with our experimental measurements of growth on amino acids (Fig. S13G).

To test these predictions, we shifted MG1655 cells from 27 °C to 37 °C during growth on casamino acids (Methods). With 4.6 mM CAA, a concentration near the K_M (Fig. S13C), growth rate increased from the steady state value at 27 °C (~0.5 h^{-1}) to that at 37 °C (~0.8 h^{-1}) after only 25 min, corresponding to 0.25 doubling times at 37 °C (Fig. 6K,L). Moreover, the spike peaked at a growth rate close to that of the 37 °C steady state (Fig. 6K). These dynamics were in reasonable agreement with the predictions of our model (Fig. 6I,J), indicating that the response to temperature shift can be modulated by nutrient concentration, owing to the properties of the import K_M.

Temperature shifts in fission yeast produce a distinct response from bacteria that is captured by the TSEN model

Diverse bacterial species, including *E. coli* from host organisms with distinct temperature-dependent evolutionary histories (turtle, seagull, human) and the soil-dwelling gram-positive *Bacillus subtilis*, exhibited similar responses to upshifts as *E. coli* MG1655 (Fig. 7A,B, S14), suggesting a general behavior across the bacterial kingdom. We sought to determine if single-celled eukaryotes would respond to temperature shifts in a similar manner. The rod-shaped fission yeast *Schizosaccharomyces pombe* grows optimally at 32 °C and possesses an Arrhenius range between 22 °C and 32 °C, with E_a~8 kcal/mol in rich media[61]. During an upshift on the rich medium YE5S from 22 °C to 32 °C, cells exhibited a large growth-rate spike from 0.17 h^{-1} to 0.44 h^{-1}, overshooting the steady-state growth rate at 32 °C (Fig. 7C). This spike was immediately followed by a deceleration to 0.02 h^{-1}, followed by rapid acceleration to the steady-state growth rate

494 at 32 °C (~0.4 h^{-1}) (Fig. 7C). The entire response dynamics lasted ~100 min,
495 corresponding to a normalized response time of ~1.1 doublings (Fig. 7D). Thus, despite
496 decelerating to near growth halting, *S. pombe* cells were able to reach the steady-state
497 growth rate at the higher temperature more quickly than any bacteria tested at
498 saturating nutrient concentration.
499
500 We wondered whether these differences in behavior were consistent with our TSEN
501 model. By systematically varying parameters, we found that enzyme networks exhibited
502 a faster normalized response time when the E_a of the bottleneck K_M was increased
503 to >30 kcal/mol and the bottleneck enzymatic rate was greater than those of import and
504 growth. Moreover, a TSEN composed of 5 bottlenecked intermediate reactions resulted
505 in a more pronounced spike and deceleration (Fig. 7D), similar to our experimental
506 measurements (Fig. 7C,D). The large spike and deceleration were due to rapid
507 consumption of the network's final metabolite (c_6), which could only be replenished by
508 upstream bottlenecked metabolites (Fig. 7E). The overall faster response time was
509 captured by the model and was due to the decrease in steady-state concentration of c_6
510 at higher temperature caused by the large E_a of K_M (Fig. 7E), leading c_6 (which is
511 limiting for growth) to stabilize more quickly.
512
513 With the same set of parameters, this TSEN model also predicted an under-shooting to
514 below the new steady-state growth rate upon a temperature decrease from 32 °C to
515 22 °C (Fig. 7F), a nonintuitive behavior we confirmed experimentally (Fig. 7F). These
516 findings suggest that the qualitatively distinct characteristics of the *S. pombe*

temperature shift responses can be captured in a TSEN model by increasing the magnitude of K_M parameters and the number of bottleneck reactions, and more generally that the growth network can be tuned to alter the balance between certain tradeoffs, to accelerate responses at the cost of temporary growth stalling.

521 **Discussion**

522 Here, we used high-precision temperature control and single-cell analyses to show that
523 bacteria exhibit a characteristic growth-rate response to temperature shifts within the
524 Arrhenius range (Fig. 1C, 7A). The maintenance of the proteome across temperatures
525 (Fig. 2) and the conservation of response dynamics during upshifts across mutants (Fig.
526 2G, 5E, S10I) and antibiotic treatments (Fig. 3H, S11B,D) collectively argue against the
527 existence of a single regulator of growth rate across Arrhenius temperatures. Instead,
528 the ability of our TSEN model to recapitulate nearly all observed behaviors (Fig. 5,6,
529 S12) indicates that temperature sensitivity of growth is a collective property of the
530 metabolic network, which encodes a memory of temperature states (Fig. 1I, S6, 6C). At
531 steady state, the TSEN model predicts that growth depends only on substrate import
532 kinetics and the total intracellular metabolite pool (Eq. 3), recovering the empirical
533 Monod Equation (Eq. 4) and providing a simple framework that connects concentration-
534 dependent growth directly to measured transporter kinetics[57]. Thus, our work
535 establishes a mechanism for how Arrhenius-like growth arises across organisms[10] (Fig.
536 1A, S1, S2, S12G).

537

538 A key feature is the temperature dependence of K_M, which provides a straightforward
539 mechanism for the asymmetry between upshift and downshift responses (Fig. 7F): if the
540 substrate concentration of a reaction is near the K_M at 27 °C (Fig. 7F, blue circle), an
541 upshift to 37 °C will be accompanied by a small instantaneous growth rate increase
542 since K_M is higher at 37 °C versus 27 °C; vice versa, a downshift from the K_M at 37 °C
543 (Fig. 7F, red circle) will result in a larger instantaneous change in growth rate (Fig. 7F).

544 Each of these instantaneous changes is then followed by an increase (upshift) or
545 decrease (downshift) in the substrate concentration, and thus the growth rate (Fig. 7F),
546 as predicted by the TSEN model (Fig. 5E, SI). The temperature upshift response is
547 predicted to be largely insensitive to the K_M of import at substrate saturation (Fig. 6F),
548 suggesting that temperature-shift responses are independent of the details of import
549 kinetics. A temperature-sensitive K_M predicts that the E_a of growth rate decreases with
550 substrate concentration[12] (Fig. 6H), consistent with our measurements of growth on
551 amino acids (Fig. S13G). Such a decrease in temperature sensitivity at low substrate
552 concentration is predicted by the TSEN to decrease the response time and increase the
553 relative spike height (Fig. 6F,G,I,J), consistent with our experimental observations that
554 decreases in amino acid concentrations resulted in faster responses to temperature
555 upshifts and larger relative spikes (Fig. 6K,L). Thus, microorganisms confronting
556 nutrient-poor environments may exhibit less temperature sensitivity of growth,
557 somewhat paradoxically owing to the temperature sensitivity of K_M values.
558
559 To produce the observed initial spike in growth rate, a bottleneck reaction with a large
560 and highly temperature-sensitive K_M was required (Fig. 5C). Previous measurements of
561 intracellular metabolite dynamics in *E. coli* grown on glucose showed that reactions in
562 central carbon metabolism are largely unsaturated and many reactions can exhibit large
563 K_M values (>1 mM)[59] (Fig. 7G), indicating that the existence of such bottlenecks is
564 highly likely. There are many potential bottleneck enzymes (Fig. 7G); those with the
565 largest substrate concentrations are involved in aspartate consumption for amino acid
566 (*aspC*) and pyrimidine (*pyrB*) biosynthesis, while those with the largest K_M are involved

567 in threonine (*ilvA*) and serine *(sdaA*, *ydfG)* degradation. As several of these reactions
568 are essential, elucidating which reactions are true bottlenecks will likely require a
569 combination of CRISPRi manipulation of gene expression, direct measurements of
570 intracellular metabolite concentrations[59], and biochemical characterization across
571 temperatures.
572
573 Additionally, the TSEN model was able to explain qualitatively distinct temperature shift
574 responses in the fission yeast *S. pombe*, which responded to an upshift with
575 overshooting and deceleration (Fig. 7C), but which ultimately reached its steady-state
576 growth rate faster than bacteria (Fig. 7D). The TSEN model predicted that large,
577 coupled bottleneck reactions account for this behavior (Fig. 7D,E), and such a model
578 predicted the undershoot response to a temperature downshift (Fig. 7F). In this
579 scenario, faster temperature-shift responses come at the cost of increasing the
580 activation energy of growth (Fig. 7C,F), further suggesting tradeoffs between fast
581 steady-state growth across temperatures and the ability to respond quickly to shifts
582 between temperatures.
583
584 Taken together, these findings suggest that metabolite flux rather than proteome
585 rearrangement underlies growth rate adaptation across Arrhenius temperatures. As a
586 result, cells adapt to temperature fluctuations without additional protein synthesis,
587 resulting in transient memory of previously experienced temperatures (Fig. 2I, S7, 6C–
588 E). Proteins comprise ~55% of the cell's biomass[62] but constitute a relatively small total
589 concentration ~7 mM[59] compared with metabolites, which make up ~300 mM despite

being only ~3% of biomass[59,62]. Thus, increasing protein concentrations is metabolically expensive, and simulations of our TSEN model explicitly including protein synthesis confirmed that enzyme concentrations remain virtually constant throughout temperature shifts (Fig. S15). The conservation of growth rate responses across organisms (Fig. 7A–D), and the ability of the TSEN model to capture diverse responses to temperature shifts (Fig. 5–7) suggests an evolutionary pressure to adopt this strategy. The ability of *E. coli* cells to withstand fluctuations across a large range of temperatures, even short pulses at heat- and cold-shock temperatures (Fig. S7B,C,E), indicates a robustness that may be particularly important in the context of host colonization and infection-induced fevers, and our findings indicate that investigations of temperature adaptation can provide key insight into the metabolic factors limiting growth.

Acknowledgements

We thank members of the Huang lab for helpful discussions. The *E. coli* BW25113 transposon mutant library was provided by the Deutschbauer lab, with help from Valentine Trotter. This work was funded by a Stanford Interdisciplinary Graduate Fellowship (to B.D.K.), NIH RM1 GM135102 (to K.C.H.) and NSF Awards EF-2125383 and IOS-2032985 (to K.C.H.). K.C.H. is a Chan Zuckerberg Biohub Investigator.

608 **Methods**

609

610 **Culturing conditions and bacterial strains**

611 *E. coli* wild-type and isolate strains were grown directly from 25% glycerol stocks stored
612 at -80 °C in target media without selection. In typical temperature upshift experiments,
613 cells were grown initially at 37 °C from frozen stocks overnight until saturation, then
614 diluted 1:200 into fresh media at 37 °C until log phase (1.5–2 h in LB, ~4 h in MOPS +
615 glucose). Cells were then diluted 1:10 into fresh media and grown for at least 3
616 doublings at the lower, target temperature before performing a temperature upshift.

617

618 Most mutants (e.g., Keio collection knockouts) were grown from frozen stocks in target
619 media with antibiotic selection. The ppGpp null strain (*spoT::cat, relA::kan*) was grown
620 on LB plates with 10 µg/mL chloramphenicol and 25 µg/mL kanamycin overnight at
621 37 °C, and individual colonies were selected for further liquid culturing under selection
622 to avoid suppressor mutations.

623

624 To evaluate growth kinetics on various media, *E. coli* MG1655 was first grown shaking
625 overnight at 37 °C in MOPS minimal medium (Teknova, Hollister, CA) adjusted to pH
626 7.2 supplemented with 0.2% (w/v) D-glucose. To measure growth at lower temperatures
627 (25 °C, 30 °C), cells were then diluted 1:200 in fresh MOPS+glucose and grown shaking
628 until saturation for an initial passage at the target temperature. One milliliter of cells
629 were washed in MOPS buffer (pH 7.2) at room temperature and 1 µL was added to 200

630 μL of target medium in 96-well plates for generating growth curves at the target
631 temperature in a plate reader.
632
633 All strains used in this study are listed in Table S1.
634
635 **Liquid growth curves and analysis**
636 Growth curves were measured using a protocol developed for accurately determining
637 growth rates at low optical density[63]. Briefly, 200 μL of medium (without bacteria) were
638 placed into each well of a transparent 96-well plate (Greiner Bio-One, Monroe, NC) and
639 sealed with a transparent film (Excel Scientific, Victorville, CA) with holes for gas
640 exchange cut above each well using a laser cutter (Epilog, Golden, CO). Optical density
641 (OD) was measured with a BioTek Epoch 2 microplate spectrophotometer (Agilent,
642 Santa Clara, CA) for at least 15 min to obtain blank values for each well at the target
643 temperature. The seal was then removed, bacterial samples were added into each well,
644 and the plate was sealed with a fresh laser-cut transparent film. Linear and orbital
645 shaking were conducted between OD readings, which were taken every ~7 min. The
646 OD was corrected for non-linearity (linear range = 0–0.6) via a serial dilution of
647 concentrated cells and performing a polynomial fit to obtain general fit parameters [63].
648 For each well, the well-specific blank OD value determined prior to addition of cells was
649 subtracted from the OD at each time point, which was then used to computed growth
650 rate as a moving linear regression of the logarithm of the blanked OD.
651
652 ***E. coli* natural isolates**

653 *E. coli* strains from non-human hosts were previously isolated[30,31,64] from fecal samples
654 collected from a variety of sources, including park and pet store animals and domestic
655 pets, which were grown on Colilert-18 medium (IDEXX, Portland, ME) for selection of
656 presumptive *E. coli* colonies[31]. Isolate identities were confirmed by beta-glucuronidase
657 activity and subsequent sequencing of the corresponding gene, *uidA*[31]. The strains were
658 grown overnight in a rich medium (LB) at 37 °C, diluted 1:200 in fresh LB, and grown for
659 24 h across temperatures from 27 °C–47 °C to measure activation energies.
660

661 **Temperature-controlled single-cell imaging**

662 The temperature control platform, the Single-Cell Temperature Controller (SiCTeC),
663 was designed and described previously[32]. Briefly, a ring-shaped Peltier module (TE
664 Technology, Traverse City, MI) was adhered to a glass slide, and the sample
665 temperature was monitored on the coverslip and controlled using a micro-Arduino with a
666 proportional-integral-derivative (PID) algorithm. Sample temperature was monitored and
667 visualized in real time using the open-source software Processing[65]. Agarose hydrogels
668 were prepared by boiling 3% ultrapure agarose (Sigma Aldrich, St. Louis, MO) in the
669 target medium, and 200 μL of the mixture were pipetted onto a 9-mm diameter silicone
670 gasket (Grace Bio-Labs, Bend, OR) onto the temperature-controlled glass slide. An
671 additional slide was placed on the gasket to compress the hydrogel, which then cooled
672 and solidified at the initial temperature of the experiment. After removing the additional
673 compressing slide, 1 μL of cells was pipetted onto the solidified hydrogel and dried
674 briefly (<1 min) at the initial temperature of the experiment.
675

676 Imaging was performed on a Ti-Eclipse microscope in phase-contrast mode using a
677 40X Ph2 air objective (NA: 0.95) (Nikon Instruments, Tokyo, Japan) with a 1.5X tube
678 lens. The air objective was used to avoid heatsink issues with oil-immersion objectives.
679 Images were captured every 30 s on a Zyla 4.2 sCMOS (Andor Technology, Belfast,
680 UK), Neo 5.5 sCMOS (Andor Technology, Belfast, UK) or PCO Panda 4.2 (Excelitas,
681 Pleasanton, CA) scientific camera. The microscope system was integrated using
682 μManager 1.41[66].
683
684 **Image analysis**
685 To extract cell morphology information throughout the experiment, subpixel-resolution
686 cellular contours were obtained through a combination of deep learning-based and
687 traditional image segmentation software[32,67]. Briefly, we first aligned the images using
688 the Template-Matching plugin in FIJI[68,69], then each image was processed with a fully
689 convolutional neural network model, *DeepCell*[67]. Separate neural networks were trained
690 for *E. coli* rich medium, *E. coli* minimal medium, and *S. pombe* rich medium, with >200
691 cells manually annotated in each condition[32,67,70]. Outputs from DeepCell classification
692 were used to extract cellular contours using *Morphometrics* v. 1.1 in MATLAB
693 (MathWorks, Natick, MA)[71]. Custom MATLAB scripts were used to track individual cells
694 and measure cellular geometry[70].
695
696 **Rapid temperature downshifts**
697 To increase the rate of temperature change during downshifts from previous
698 experiments performed using ambient temperature as the cooling sink, which required

699 ~5 min from 37°C to 27 °C[32], we used dry ice (solid CO_2) to rapidly cool samples.
700 During a downshift, the SiCTeC device was powered off and a 250-mL beaker with dry
701 ice was used to pour sublimating dry ice directly onto the sample on the glass slide. For
702 downshifts to temperatures above ambient, when the temperature was ~1 °C above the
703 target downshift temperature, the SiCTeC device was powered back on and the PID
704 algorithm restarted control of the sample temperature. The sample temperature was
705 closely monitored and adjusted accordingly for undershooting. This method enabled
706 stabiliziation at the lower temperature within <1 min. For downshifts to temperatures
707 below ambient, dry ice was continuously poured onto the sample at intervals necessary
708 to maintain the target temperature. Temperature upshifts back to 37 °C were performed
709 by turning back on the SiCTeC device.
710

711 **Anaerobic growth**

712 To perform temperature shifts in anerobic conditions, *E. coli* MG1655 was inoculated
713 from a frozen stock into LB and grown overnight in an anaerobic chamber (Coy
714 Laboratory Products, Grass Lake, MI), then diluted 1:200 and grown until saturation in
715 pre-reduced LB (i.e., kept in chamber for >48 h before culturing). Cells were diluted
716 1:200 in pre-reduced LB and grown at 37 °C until log phase (~2 h), then diluted 1:10
717 and grown at 27 °C for 3 h. From log phase at 27 °C, 1 μL was pipetted on a SiCTeC
718 glass slide for temperature shifts (all components pre-reduced) and imaged inside the
719 chamber using a Ti-Eclipse inverted microscope (Nikon Instruments, Tokyo, Japan) with
720 a Neo 5.5 sCMOS (Andor Technology, Belfast, UK). The SiCTeC platform was
721 controlled by a laptop inside the chamber.

722

723 **Quantification of response time**

724 To measure the response time of an upshift trajectory, the steady-state growth rate (g^{ss})
725 at the final temperature was determined by measuring the average of the growth rate
726 across the timepoints after which growth rate had stabilized (determined by visual
727 inspection). Its error (δg^{ss}) is defined as the standard error of the mean. This steady-
728 state growth rate was subtracted from the entire trajectory ($g(t) - g^{ss}$), and the
729 response time was determined as the time (t) at which $g(t)$ was indistinguishable from
730 g^{ss} within error (δg^{ss}), which was generally ~5% of g^{ss}.

731

732 **Antibiotic treatment during single-cell temperature shifts**

733 Five-hundred microliter aliquots of growth medium+3% ultrapure agarose were melted
734 at 95 °C, then mixed with 0.5 μL of 1000X target concentration antibiotic stock solution
735 and 150 μL was immediately used to make a hydrogel for the sample as described
736 above. The short time exposed to higher temperatures (~30 s) likely only moderately
737 impacted the minimum inhibitory concentration, as antibiotic efficacies against *E. coli*
738 are unaffected by long-term (30 min) treatment at 56 °C, with many drugs unaffected by
739 autoclaving (121 °C)[72].

740

741 **Liquid culture samples for proteome extraction**

742 *E. coli* MG1655 was grown at 37 °C overnight in MOPS buffer (Teknova, Hollister, CA)
743 adjusted to pH 7.2 supplemented with 0.2% (w/v) of carbon source (glucose or glycerol)
744 (Sigma-Aldrich, St. Louis, MO) or LB (Thermo Fisher Scientific, Waltham, MA), then

745 diluted in duplicate and grown for at least 4 doublings at the target temperature (25 °C,
746 30 °C, or 37 °C). Growth at additional temperatures (16 °C, 43 °C) were assayed for LB.
747 Cultures were grown to log phase (OD_{600}~0.2) in 50-mL Falcon tubes and 15 mL were
748 harvested and washed with 1 mL PBS via centrifugation at 4 °C. Supernatant was
749 removed and the pellet was snap-frozen with liquid nitrogen.
750

751 **Proteome extraction**

752 Extraction was performed as previously described[73]. Briefly, samples were thawed and
753 lysed using a bead-beating procedure, then supernatant was reduced and alkylated with
754 DTT and iodoacetamide, respectively. Peptides were then washed, digested, and eluted
755 using S-trap tubes (Protifi) and desalted with C18 solid-phase extraction (Sep-Pak
756 Waters). Finally, peptides were dried by vacuum centrifugation and quantified for
757 normalization (Nanodrop ND-1000).
758

759 **Proteomic analysis via LC-MS/MS and database searching**

760 Peptide quantification was performed as previously described[73]. Briefly, dried peptides
761 were diluted in 0.2% formic acid to a final concentration of 0.5 μg/mL, then separated by
762 reversed-phase chromatography (Dionex Ultimate 3000 HPLC, Thermo Fisher
763 Scientific, Waltham, MA) and directed to a LTQ Orbitrap Elite mass spectrometer
764 (Thermo Fisher Scientific, Waltham, MA). The top 20 ions were selected for
765 fragmentation using collision-induced dissociation (DIC), and fragments were analyzed
766 in the ion trap with rapid scan rate.
767

768 Mass spectra were searched against the UniProt canonical *E. coli* FASTA database
769 using the SEQUEST algorithm of Proteome Discoverer 2.2.0.388. Peptides were filtered
770 using Percolator with the protein false discovery rate set to 1%. Protein abundance was
771 based on precursor ion peak areas.
772

773 **Proteome data analysis and annotation using Clusters of Orthologous Groups**
774 **(COG)**

775 Protein functional annotation was performed using the Clusters of Orthologous Groups
776 of proteins (COG) database[42]. UniProt accession codes were mapped to the COG
777 database downloaded from https://ftp.ncbi.nih.gov/pub/COG/COG2014/data/. After
778 removing non-bacterial groups, COGs were reduced to 9 functional groups: ribosomal
779 protein (RP), non-RP translational, transcription, DNA replication, cell division, cell
780 envelope structure, post-translational modification, energy and metabolism, and other.
781 The corresponding gene of each protein was annotated using the gene association
782 table from EcoCyc (https://ecoliwiki.org/gaf/gene_association.ecocyc.gz)[74]. Further
783 analysis was performed using custom MATLAB scripts, wherein the relative abundance
784 of each protein was calculated for each sample and its replicates and then compared
785 across conditions.
786

787 ***E. coli* transposon library temperature shifts**

788 One milliliter of a pooled library of *E. coli* BW25113 transposon insertion mutants with
789 random DNA barcodes[44] was thawed and diluted into 50 mL of LB+25 μg/mL
790 kanamycin (Sigma Aldrich, St. Louis, MO) in a 250-mL Erlenmeyer flask (Pyrex,

791 Glendale, AZ) and grown shaking overnight at 37 °C. 0.5 mL of the stationary-phase
792 library cultures were diluted into 50 mL of LB in technical replicates at 25 °C and 37 °C.
793
794 The 25 °C culture was grown for 3 h to early log phase (OD_{600}~0.15) and 6 mL were
795 diluted into in each of two flasks containing 50 mL fresh LB pre-warmed at 25 °C, then
796 grown for another 3 h in an air-heated shaker (New Brunswick Scientific, Edison, NJ).
797 The temperature upshift from 25 °C to 37 °C was performed by placing one of the 25 °C
798 flasks into a heated water shaker at 37 °C. The control sample was left at 25 °C.
799 Samples were collected in 1.5-mL aliquots and flash-frozen using liquid nitrogen every
800 10 min at timepoints of -10, 0, 10, 20, 30, 40, 60, 90 min relative to the shift (control
801 samples without temperature shifts were also taken at the same time points).
802
803 The 37 °C culture was grown for 2 h until mid- to late-log phase (OD_{600}~0.3) and 1.5 mL
804 were diluted into each of two flasks containing 50 mL of fresh LB pre-warmed at 37 °C,
805 then grown for ~1 h in a heated water shaker. For the temperature downshift from 37 °C
806 to 25 °C, one of the flasks was first placed into a room-temperature water bath for 6 min
807 for faster cooling, then transferred to an air-heated shaker at 25 °C. The other flask was
808 maintained at 37 °C as a control.
809
810 Each set of downshift/upshift experiments was performed twice, and all samples were
811 flash frozen and immediately stored at -80 °C. Optical density was monitored at each
812 time point for all experiments with a Genesys 20 spectrophotometer (Thermo Fisher
813 Scientific, Waltham, MA). The time scale of the temperature upshift was estimated to be

814 ~3.5 min using a virtual experiment with 50 mL of water in a flask, whose temperature
815 was directly monitored during a shift from 25 °C to 37 °C using the SiCTeC device
816 thermistor reading. A similar test was performed for the 37 °C to 25 °C downshift by
817 placing a 37 °C flask with 50 mL of water into a stationary water bath at room
818 temperature, giving an estimate of ~6 min to complete the temperature shift.
819

820 ***E. coli* transposon mutant library sequencing and analysis**

821 Barcode sequencing (BarSeq) was performed as previously described[44]. Briefly,
822 genomic DNA was extracted using the DNeasy 96 Blood and Tissue kit (Qiagen) and
823 quantified using the Quant-iT dsDNA BR Assay kit (Qiagen). BarSeq PCR was
824 performed using 200 ng of genomic DNA template in 150-μL reaction volumes with Q5
825 polymerase (with enhancer) (New England Biolabs, Ipswich, MA), 20 μM universal
826 forward P5 primer, and 20 μM reverse P7 primers with 6-bp TruSeq indices that are
827 automatically demultiplexed by Illumina software. PCR products were checked for
828 completion using gel electrophoresis, and 10 μL of each reaction product were pooled
829 and purified using the Zymo DNA Clean and Concentrator kit (Zymo Research, Irvine,
830 CA). Sequencing was performed at the Chan Zuckerberg BioHub facility on an Illumina
831 NextSeq 550 platform in High Output mode.
832

833 BarSeq analysis was performed as previously detailed[44], with relevant scripts at
834 https://genomics.lbl.gov/supplemental/rbarseq/. Briefly, barcode reads were mapped to
835 their corresponding genomic loci using sequencing of the transposon insertions in the *E.*
836 *coli* library, and genes were filtered for those with ≥10 barcodes in the central (10–90%)

837 portion of the gene. Temperature-shift samples were analyzed along with their
838 corresponding unshifted control samples, with the time-zero sample corresponding to
839 when the library was shifted (*t*=0 sample). The fitness of each mutant was measured as
840 the $\log_2$ fold-change in its relative abundance, and further analysis was performed using
841 custom MATLAB scripts.
842
843 **FRAP measurements**
844 *E. coli* cultures were grown overnight from frozen stocks at 37 °C in LB, with 25 µg/mL
845 kanamycin selection for Δ*fabR* and Δ*fadR* mutants, and then diluted 1:200 into fresh LB
846 and grown until log phase at 37 °C (~2 h). Cultures were then diluted 1:10 into fresh LB,
847 and 2 µL of 0.5 mg/mL MitoTracker Green (Thermo Fisher Scientific, Waltham, MA)
848 were added. The culture was grown at the target temperature for 30 min to enable
849 sufficient membrane labeling. Five hundred microliters of stained cells were washed via
850 centrifugation (30 s at 7000 rcf) in fresh LB at the target temperature (37 °C or 27 °C).
851 One microliter of washed culture was placed on an LB 3% agarose hydrogel and
852 prepared for imaging using standard glass slide technique. Imaging was performed with
853 a Zeiss LSM 880 confocal microscope with an environmental chamber for monitoring
854 and controlling temperature (37 °C) and integrated with the ZEN software suite (Zeiss,
855 Oberkochen, Germany). Temperature upshift experiments were performed by placing
856 the sample into the heated environmental chamber for 5 min before imaging.
857 Fluorescence recovery after photobleaching (FRAP) of individual cells was performed
858 with excitation at 488 nm using the ZEN software by choosing a photobleaching region

near cell tips covering 1/4 to 1/3 of the cell. The entire cell was imaged at minimum frame intervals (150–300 ms) to image fluorescence recovery.

FRAP analysis and viscosity estimate

Individual regions of interest were manually delineated for the photobleached cell tips and the entire cell in FIJI[69], and the total fluorescence of each area was quantified at each time point. These data were imported for further analysis in MATLAB. The fluorescence recovery in each photobleached region was corrected by the rate of photobleaching in the entire cell, and the recovery curve was normalized and fit to the exponential function $(1 - e^{-\frac{t}{\tau_D}})$. The time constant (τ_D) was used to estimate a diffusion coefficient (D) via solution to Gaussian photobleaching in a plane, $\tau_D = \frac{r^2}{4D}$ (i.e., modeling the cell tip as a disk of radius r on the membrane)[75]. The viscosity (η) was calculated using the Stokes-Einstein equation $(\eta = \frac{k_B T}{6\pi R D})$, where R is the radius of the fluorophore (estimated as 2 nm).

***Schizosaccharomyces pombe* culturing**

S. pombe WT972 h- was grown from a frozen stock on YE5S plates (5 g/L yeast extract, 30 g/L glucose, 225 mg/L each of adenine, histidine, leucine, uracil, and lysine hydrochloride, 2% Difco Bacto Agar). A single colony was grown at 22 °C or 32 °C in liquid YE5S overnight until saturation, then diluted 1:100 and grown until log phase (OD_{600}~0.3–0.5). One microliter of log-phase cells was placed on a 3% agarose YE5S pad at the initial temperature of the experiment for imaging.

882 **Estimate of LB molarity**

883 LB is largely comprised of free amino acids, and measurements of *E. coli* auxotrophy
884 and direct HPLC quantification[74] have provided an estimate of ~122 g/mol for its free
885 amino acid content. The molar mass of tryptone is reported by the manufacturer to be
886 71.08 g/mol (Thermo Fisher Scientific, Waltham, MA). As LB is composed of 10 g
887 tryptone and 5 g yeast extract dissolved in 1 L H_2O, we estimate that the concentration
888 of metabolizable free amino acids in LB is ~182 mM. Note that the accuracy of this
889 estimate is not critical for any of our conclusions; the value simply enables plotting LB
890 concentrations on the same plot as other substrates such as casamino acids.

891

892 **Measurements of K_M**

893 *E. coli* MG1655 was grown overnight until saturation in MOPS buffer+0.2% (w/v)
894 glucose at the target temperature (25 °C, 30 °C, 37 °C), then washed twice in MOPS
895 buffer before being diluted 1:200 in the target medium at the target temperature. Liquid
896 culture growth curves were obtained as described above. Optical density (OD) was
897 measured using a microplate reader and maximal growth rate was quantified as the
898 peak of the derivative of ln(background-subtracted OD)[63]. A weighted fit was performed
899 on the growth rate versus concentration curve using the Monod equation (Eq. 4) to
900 extract an estimate of K_M with a standard error. We note that it was challenging to
901 obtain growth rates at low concentration for simple sugars (e.g., glucose, fructose), due
902 to both the low K_M and generally low growth rate (<0.2 h^{-1}) (Fig. S13A–C). In succinate,
903 the relationship between ln(growth rate) and 1/*T* appeared bilinear, thus a linear fit
904 produced an estimate of E_a with very large standard error (19±14 kcal/mol) (Fig. S13G).

Figures

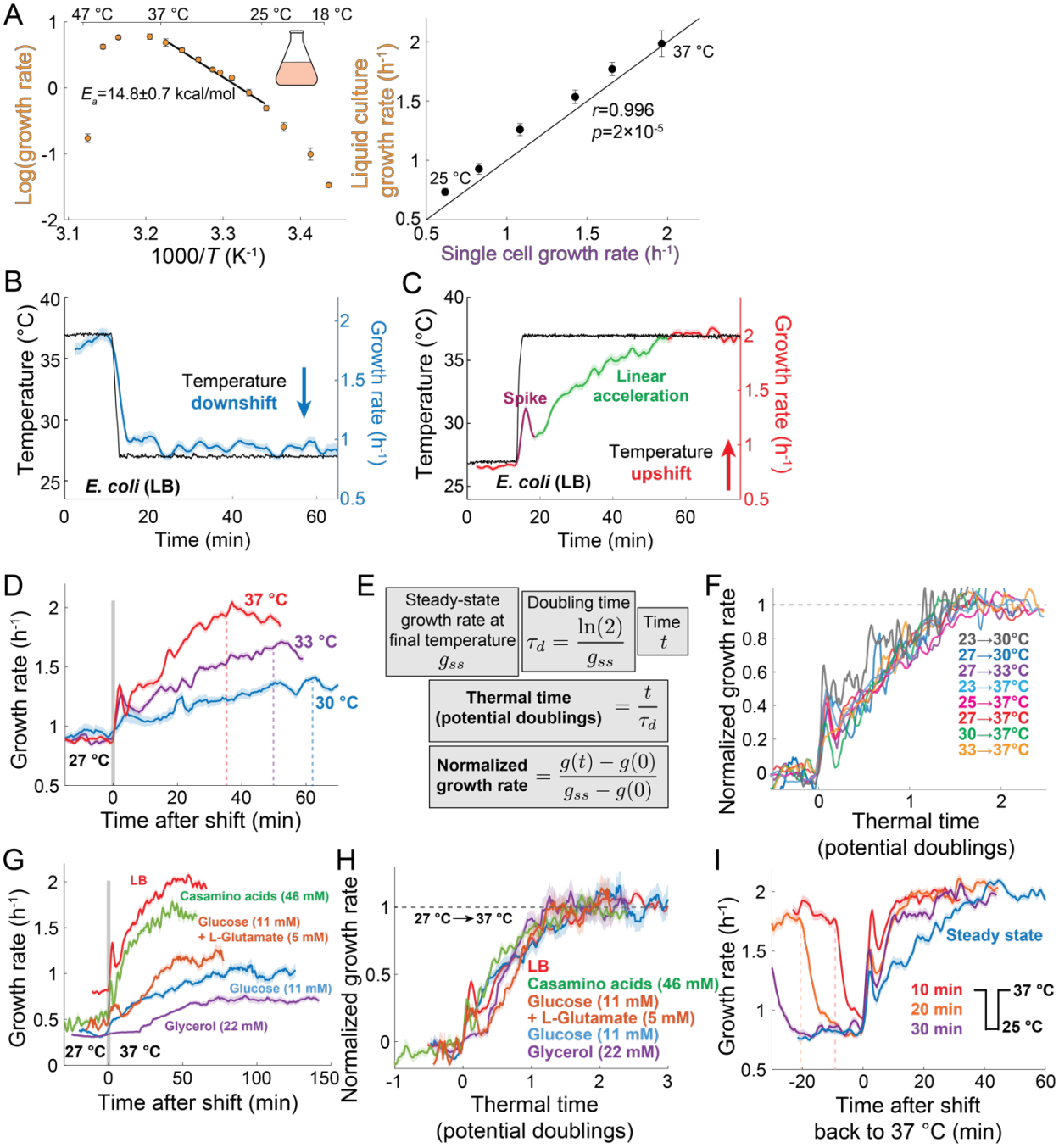

Figure 1: *E. coli* responds asymmetrically to temperature shifts, and upshift dynamics are determined by the steady-state growth rate at the final temperature.

A) (Left) Arrhenius plot illustrating that the natural logarithm of *E. coli* MG1655 maximal growth rate for temperatures between 25 °C and 37 °C varies linearly with the inverse absolute temperature, with a negative slope whose magnitude is the activation energy (E_a). (Right) Liquid-culture and single-cell growth rates were highly correlated for temperatures in the Arrhenius range between 25 °C and 37 °C (data from Fig. S1C,E).

B) Single-cell growth rate (blue) of *E. coli* MG1655 throughout a temperature (black) downshift from 37 °C to 27 °C in rich growth medium (LB) (n=253 cells). The curve is the mean growth rate and the shaded region represents one standard error of the mean (SEM) Growth rate responds quickly to the downshift.

C) Single-cell growth rate (red) of *E. coli* MG1655 throughout a temperature (black) upshift from 27 °C to 37 °C in LB (n=792 cells). The curve is the mean growth rate and the shaded regions represent ±1 SEM. Growth rate initially spikes (dark red), followed by linear acceleration (green) to the new steady-state value over ~35 min.

D) Single-cell growth rate of *E. coli* MG1655 throughout a temperature upshift from 27 °C to 30 °C (blue, n=253 cells), 33 °C (purple, n=754 cells), or 37 °C (red, n=904 cells) in LB. Vertical dashed lines indicate the time at which the growth rate reached its steady-state value at the higher temperature. Curves show the mean growth rate and the shaded regions represent ±1 SEM.

E) The thermal time is defined as the time (t) measured in units of doubling times (τ_d) of steady-state growth at the higher temperature. The normalized growth rate is defined as the difference between the growth rate at time ($g(t)$) and the growth

933 rate at the temperature shift ($g(0)$) divided by the difference between the steady-
934 state growth rate at the higher temperature (g_{ss}) and the initial temperature ($g(0)$).
935 F) Normalized single-cell growth rate of *E. coli* MG1655 grown in LB exhibits a
936 characteristic response with respect to thermal time for shifts between two
937 temperatures in the Arrhenius range 23 °C–37 °C (n=253–904 cells). Curves
938 represent the mean, and error bars have been omitted for ease of viewing.
939 G) Single-cell growth rate of *E. coli* MG1655 throughout a temperature upshift from
940 27 °C to 37 °C in LB (red, n=792 cells), casamino acids (green, n=270 cells),
941 glucose (blue, n=353 cells), glucose+glutamate (orange, n=220 cells), or glycerol
942 (purple, n=520 cells). Curves show the mean growth rate and the shaded regions
943 represent ±1 SEM.
944 H) Despite the wide variation in absolute growth-rate responses (G), normalized
945 growth rate followed an approximately conserved trajectory versus thermal time
946 across nutrient environments.
947 I) Single-cell growth rates of *E. coli* MG1655 in LB grown to steady state at 37 °C
948 and then subjected to pulses at 25 °C for 10 min (red, n=1015 cells), 20 min
949 (orange, n=1022 cells), or 30 min (purple, n=586 cells). Vertical dotted lines
950 represent the times at which cells were subjected to the downshift to 25 °C for
951 the 10- and 20-min pulses. The upshift from steady-state growth at 25 °C to
952 37 °C is also shown for comparison (blue, n=773 cells). Curves show the mean
953 growth rate and the shaded regions represent ±1 SEM.

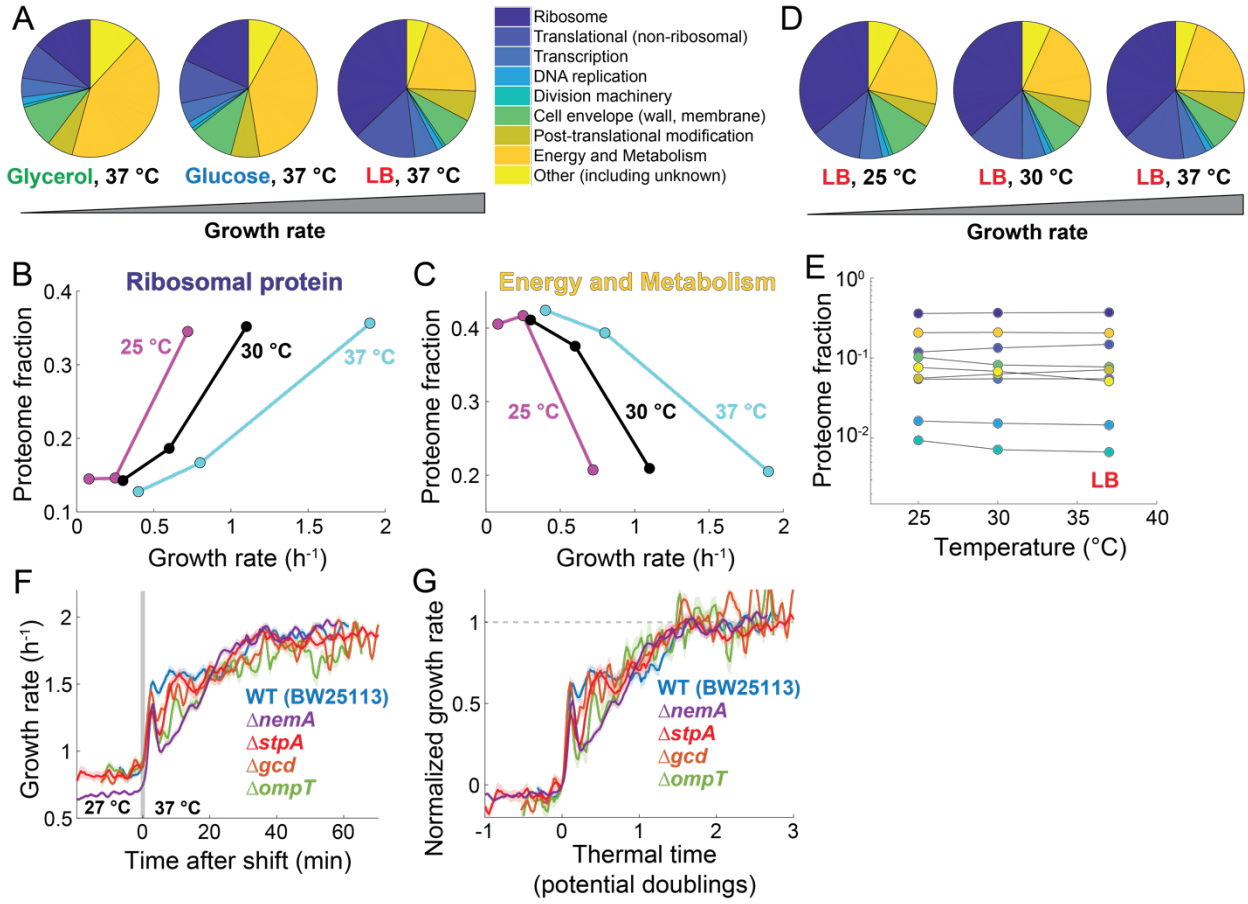

Figure 2: The delayed response to a temperature upshift is not due to proteome rearrangement.

A) The *E. coli* proteome at 37 °C varies across media. Functional proteomic sectors (pie chart) were annotated according to the Clusters of Orthologous Groups (COG) classification (Methods).

B) Ribosomal protein fraction increased with growth rate across media (M9+glycerol, M9+glucose, LB), independent of growth temperature.

C) Energy and metabolism protein fraction decreased with growth rate across media (M9+glycerol, M9+glucose, LB), independent of growth temperature.

D) The *E. coli* proteome in LB is largely invariant across temperatures in the Arrhenius range (25 °C–37 °C).

E) The proteome fraction accounted for by each functional category was approximately constant in LB across Arrhenius temperatures. Colors correspond to the functions in the legend in (A).

F) Temperature-upshift (27 °C to 37 °C) responses of individual deletion mutants of the four most abundant of the proteins whose relative abundance scaled with temperature across all media conditions. (blue: parent strain wild-type BW25113, *n*=710 cells; purple: Δ*nemA*, *n*=1052 cells; red: Δ*stpA*, *n*=588 cells; orange: Δ*gcd*, *n*=814 cells; green: Δ*ompT*, *n*=324 cells). Curves show the mean growth rate and the shaded regions represent ±1 SEM.

G) Normalized growth rate followed an approximately conserved trajectory versus thermal time across the mutant growth data in (F).

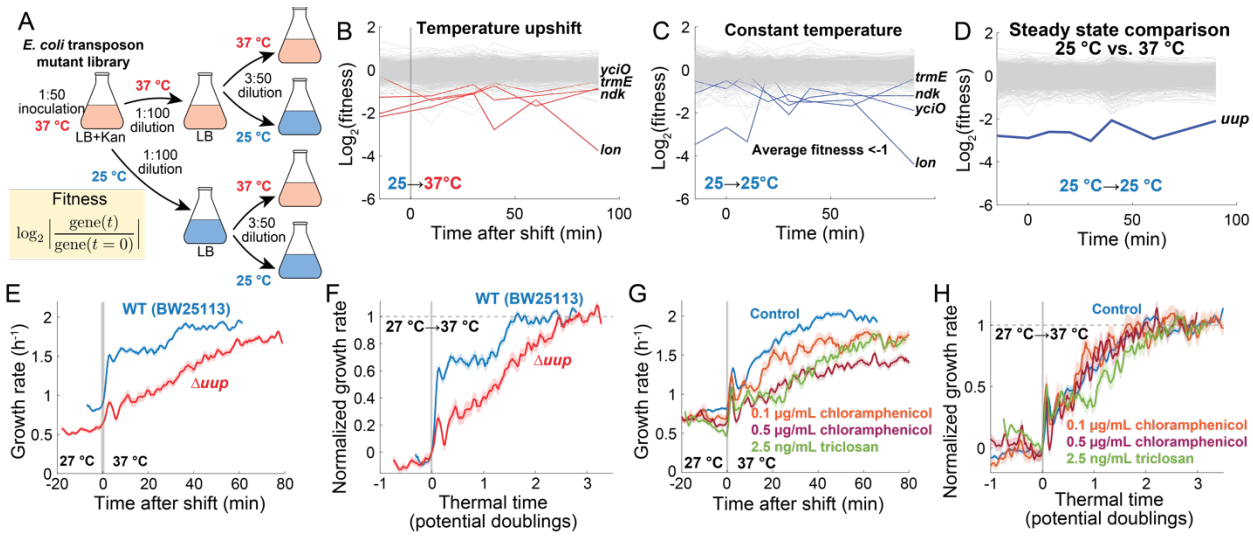

Figure 3: Response time is unaffected by almost all genetic and chemical perturbations.

A) Schematic of temperature-shift experiments screening a pooled library of *E. coli* BW25113 randomly barcoded transposon mutants (Methods). The library was initially grown in a 50-mL volume at 37 °C, then diluted and grown to steady state at the initial target temperature (25 °C or 37 °C) before shifting to 25 °C or 37 °C at time *t*=0. The optical density was monitored at each sampling time point (~10 min intervals). The fitness of each mutant is defined as the $\log_2$(relative abundance compared to *t*=0) (Methods). This experiment was carried out twice.

B) Trajectories of mutant fitness during a shift from 25 °C to 37 °C (gray vertical bar denotes timing of the shift). Mutants with fitness<-1 when averaged over time points are highlighted in red.

C) Trajectories of mutant fitness during steady-state growth at 25 °C. Mutants with fitness<-1 when averaged over time points are highlighted in blue. (B) and (C) are from the same experiment, and outlier mutants in the upshift (B) were also outliers in the control (C).

994 D) Trajectories of $\log_2$(relative abundance) during steady-state growth at 25 °C
995 compared with at 37 °C. A single gene, *uup*, had fitness<-1 when averaged over
996 time points.
997 E) Single-cell growth rate of Δ*uup* (red, *n*=609 cells) and its parent BW25113 (blue,
998 *n*=734 cells) throughout a temperature shift from 27 °C to 37 °C. Curves show
999 the mean growth rate and shaded regions represent ±1 SEM.
1000 F) Normalized growth rate versus thermal time for each trajectory in (E) shows that
1001 Δ*uup* cells respond more slowly to an upshift.
1002 G) Single-cell growth rates of *E. coli* MG1655 in LB treated with 0.1 μg/mL
1003 chloramphenicol (orange, *n*=264 cells), 0.5 μg/mL chloramphenicol (dark red,
1004 *n*=382 cells) or 2.5 ng/mL triclosan (green, *n*=266 cells) throughout a shift from
1005 27 °C to 37 °C. The untreated control is also shown for comparison (blue, *n*=792
1006 cells). Curves show the mean growth rate and shaded regions represent ±1
1007 SEM.
1008 H) Normalized growth rate followed a similar trajectory versus thermal time as the
1009 control for the chloramphenicol treatment data in (G), while triclosan slightly
1010 delayed the growth-rate response.

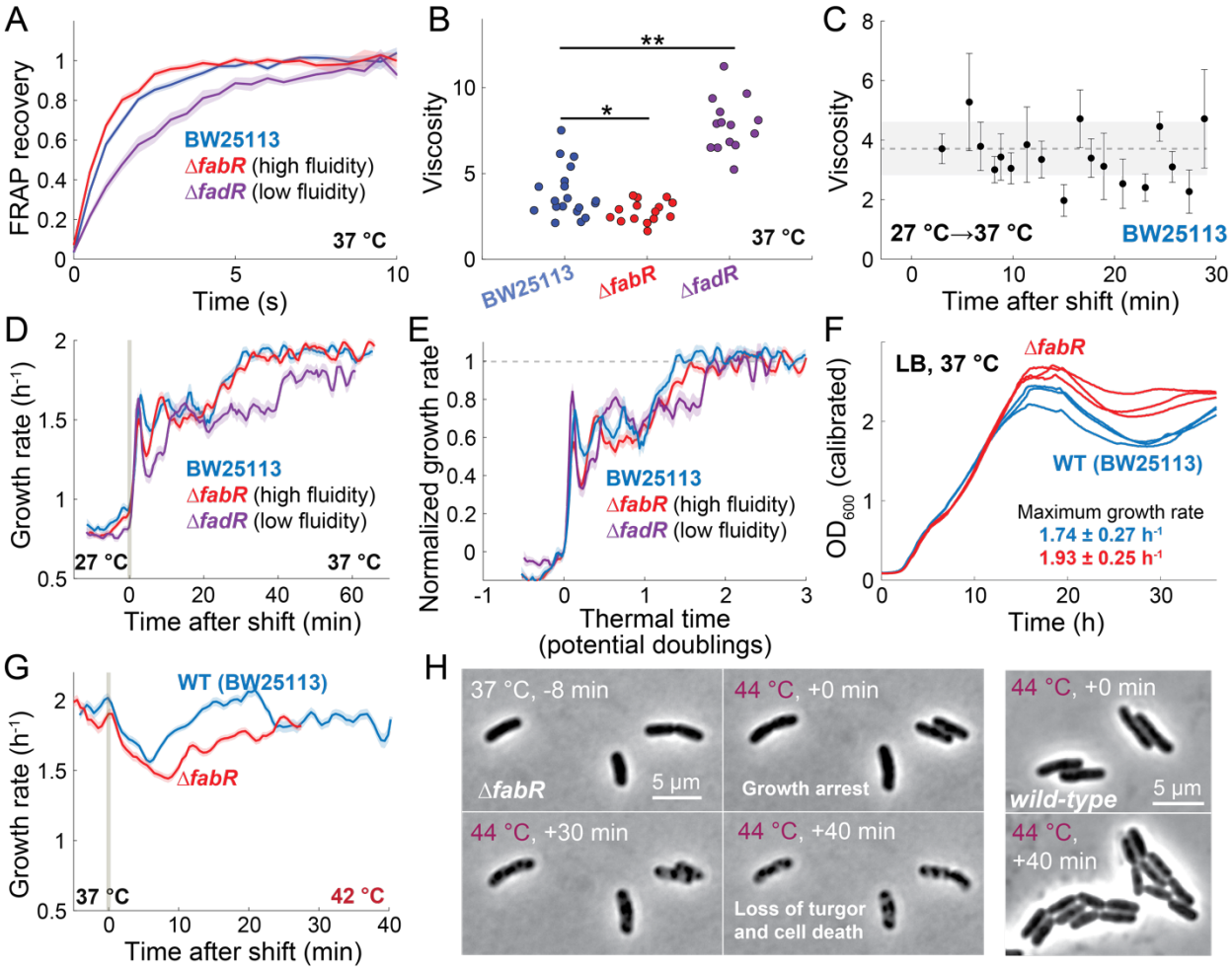

Figure 4: Changes in membrane fluidity do not alter the response to temperature upshift but increase lysis at high temperatures.

A) FRAP recovery dynamics of the membrane dye MitoTracker in the parent strain BW25113 (blue, *n*=19 cells), the high-fluidity mutant Δ*fabR* (red, *n*=15 cells), and the low-fluidity mutant Δ*fadR* (purple, *n*=14 cells) grown on LB (Methods). Curves show the mean recovery and shaded regions represent ±1 SEM.

B) Membrane viscosity (Methods) was significantly lower and higher in Δ*fabR* and Δ*fadR*, respectively, compared with the parent. Significance was determined using a two-sample t-test; *: $p<0.05$, **: $p<0.005$.

1021 C) Membrane viscosity of *E. coli* BW25113 cells after an upshift at *t*=0 from 27 °C to
1022 37 °C in LB (Methods). Points are estimates from a best fit (Methods) and error
1023 bars represent 1 standard error. Dotted line is the mean viscosity from steady-
1024 state measurements (B), and the shaded region represents ±1 standard
1025 deviation.
1026 D) Growth rate responses of *E. coli* BW25113 (blue, *n*=686 cells), Δ*fabR* (red,
1027 *n*=924 cells), and Δ*fadR* (purple, *n*=409 cells) to a temperature upshift from 27 °C
1028 to 37 °C in LB. Curves show mean growth rate and shaded regions represent ±1
1029 SEM.
1030 E) Normalized growth rate followed a similar trajectory versus thermal time among
1031 the mutants and parent for the data in (D).
1032 F) Growth curves of wild-type (BW25113) (blue) and Δ*fabR* (red) cells grown in LB
1033 at 37 °C (*n*=3 replicates). Optical density (OD) was corrected for non-linearity at
1034 high OD values (Methods). Maximum growth rates are the mean across
1035 replicates and the error is ±1 standard deviation.
1036 G) Growth rate response to a temperature upshift from 37 °C to 42 °C in *E. coli*
1037 BW25113 (blue, *n*=1011 cells) and Δ*fabR* (red, *n*=554 cells). Both strains
1038 exhibited an initial decrease in growth rate followed by recovery to the steady-
1039 state growth rate at 37 °C, but recovery was more delayed for the high-fluidity
1040 Δ*fabR* mutant. Curves show mean growth rate and shaded regions represent ±1
1041 SEM.
1042 H) (Left) Representative images of Δ*fabR* cells throughout a temperature upshift
1043 from 37 °C to 44 °C. At 37 °C, morphology and growth were wild-type-like (top

1044 left). Growth halted immediately after the shift to 44 °C (top right), with loss of
1045 turgor and cell death occurring within 30–40 min after the shift (bottom left, right).
1046 (Right) Representative images of wild-type MG1655 cells before and after an
1047 upshift from 37 °C to 44 °C. Cells maintained growth and shape.

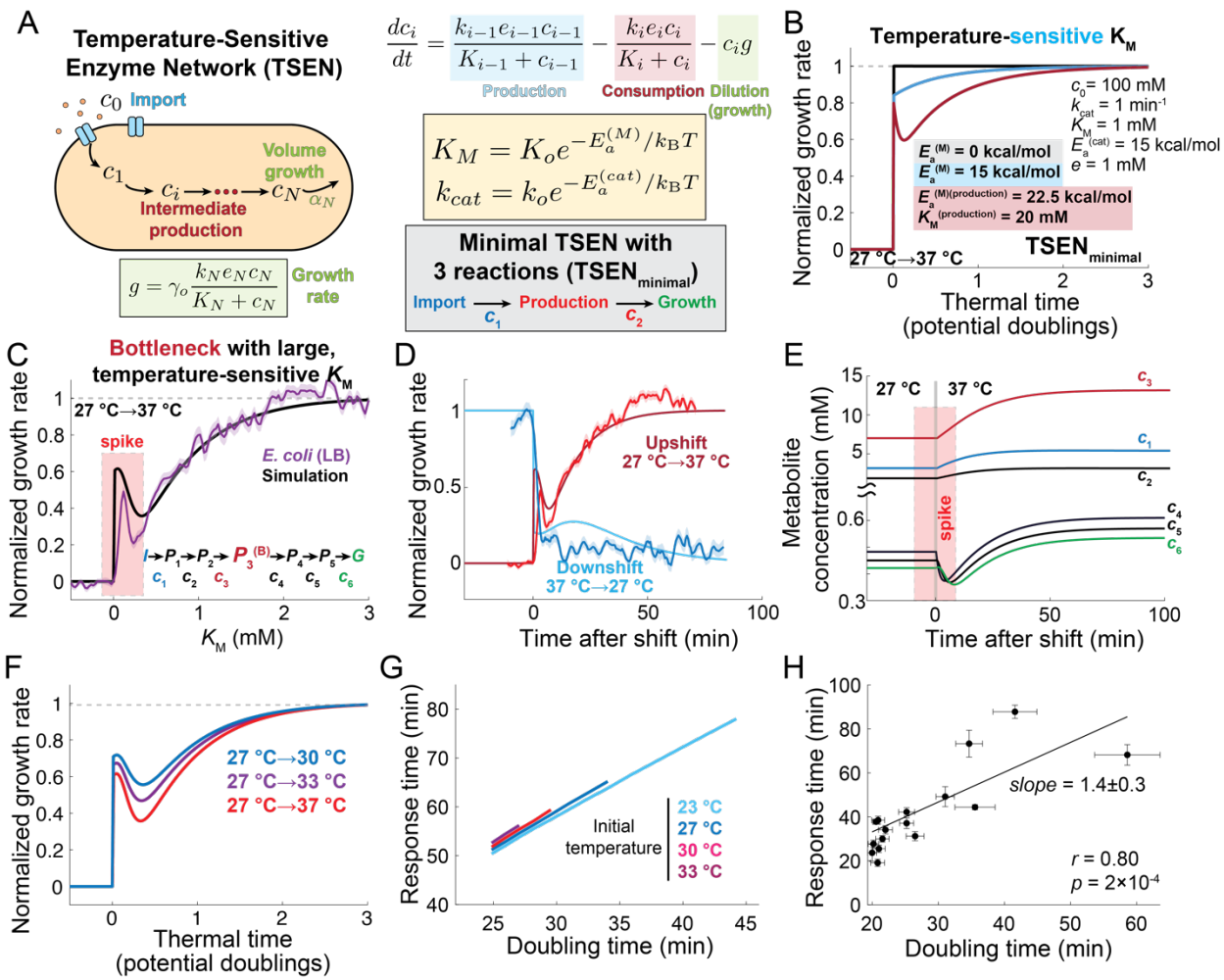

Figure 5: A temperature-sensitive enzyme network (TSEN) model recapitulates temperature-shift behaviors through metabolome rearrangement.

A) (Upper left) In the TSEN model, the import reaction (blue), production reactions (dark red), and volume growth reaction (green) are chained Michaelis-Menten reactions. (Upper right) The rate equation for each intermediate metabolite (c_i) involves enzymatic production from c_{i-1} by enzyme e_{i-1} (blue), enzymatic consumption by enzyme e_i (red), and dilution by volume growth g (green). The final intermediate c_N is translated into volume growth with an efficiency factor γ_0 (green box). Each kinetic parameter is assumed to be temperature sensitive

according to an Arrhenius equation with activation energy E_a (yellow box). A minimal TSEN model ($TSEN_{minimal}$) has a single intermediate production reaction (red), such that the network has only 2 intermediate metabolites (c_1, c_2; gray box).

B) Normalized growth rate versus thermal time from simulations of a minimal TSEN model with (blue) and without (black) a temperature-sensitive Michaelis-Menten constant (K_M) throughout a temperature shift from 27 °C to 37 °C. All other model parameters are identical and are defined in the panel inset. The TSEN with a temperature-sensitive K_M results in a non-zero response time (blue). A TSEN model with a bottleneck (dark red, $K_M = 20$ mM, $E_a = 22.5$ kcal/mol) produces an initial spike.

C) A TSEN model with a single bottleneck (red, P_3) embedded within a 7-reaction chain produces a quantitatively similar response to an upshift from 27 °C to 37 °C as *E. coli* MG1655 cells on LB (purple, *n*=792 cells; shaded region represents ±1 SEM). All other reactions have parameters identical to the minimal model without a bottleneck (blue) in (B).

D) Normalized growth rate in simulations of the bottlenecked TSEN model in (C) throughout an upshift (dark red) or downshift (light blue) between 27 °C and 37 °C. In contrast to the spike and slow response to the upshift, the downshift results in immediate deceleration to a growth rate close to the steady-state value at 27 °C, followed by slow deceleration to new steady-state value. Overlaid are the normalized growth rates of *E. coli* MG1655 subjected to an upshift (red, 27 °C

1080 to 37 °C, n=792 cells) or downshift (blue, 37 °C to 27 °C, n=253 cells). Shaded
1081 error bars represent ±1 SEM.
1082 E) The TSEN model in (C) predicts that metabolites upstream of the bottleneck
1083 ($c_{1,2,3}$) will have lower concentrations than those after the bottleneck ($c_{4,5,6}$) and
1084 increase slowly on the time scale of growth after an upshift. Post-bottleneck
1085 metabolites undergo transient decreases immediately after the temperature
1086 upshift over a time interval corresponding to the spike (red box). After this initial
1087 period, all metabolites increase to new values corresponding to the steady state
1088 at the higher temperature.
1089 F) The TSEN model in (C) predicts highly similar responses of normalized growth
1090 rate with thermal time for upshifts from 27 °C to 30 °C (blue), 33 °C (purple), or
1091 37 °C (red).
1092 G) Over a broad range of final temperatures, the absolute upshift response time
1093 (time to reach 98% of the difference between steady-state growth rates) has
1094 linear scaling with the doubling time at the final temperature. Each line
1095 represents simulations from a given initial temperature to temperatures up to
1096 37 °C.
1097 H) Experimental estimates of absolute response time follow a linear scaling with
1098 doubling time at the final temperature, similar to simulations in (G). Shown are
1099 data for upshifts involving initial and final temperatures ranging between 23 °C
1100 and 37 °C (data from Fig. 1F–H).

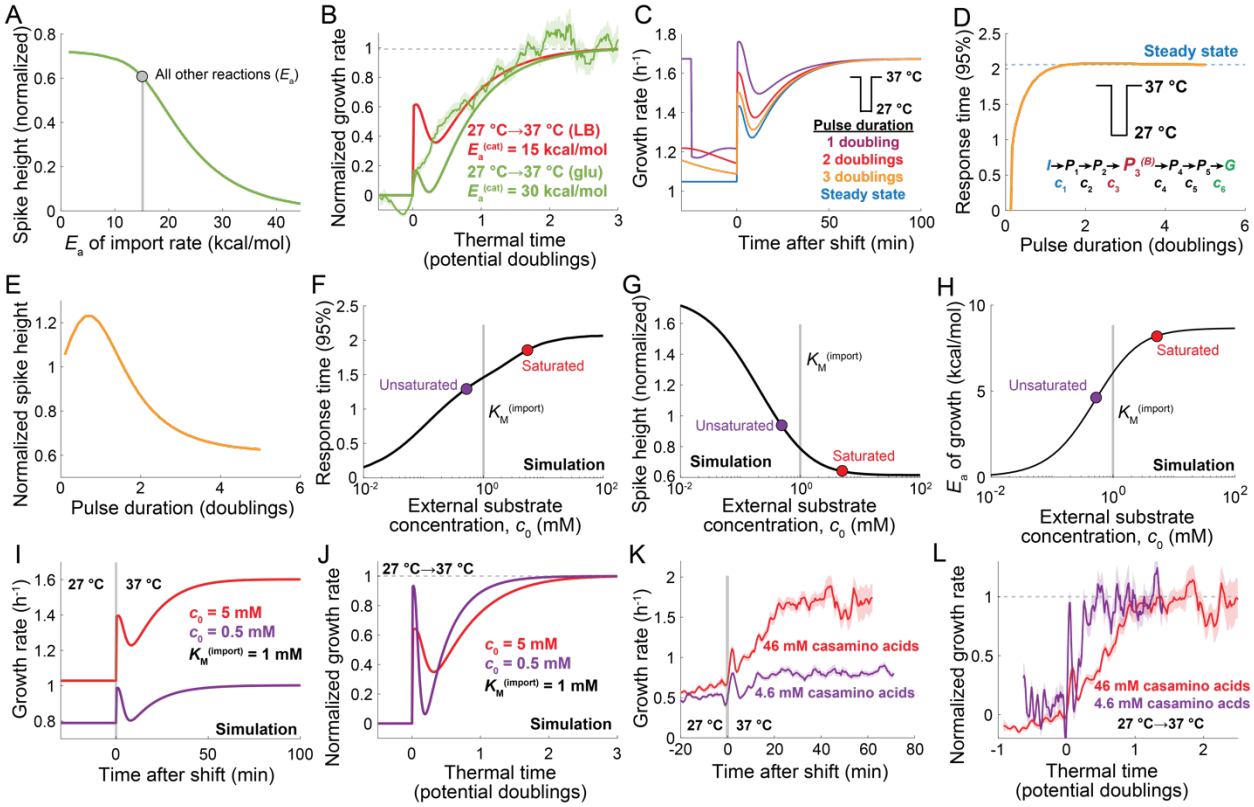

Figure 6: TSEN model predicts changes to upshift response during growth on simple sugars, after a downshift pulse, and at low nutrient concentration.

A) The bottlenecked TSEN model in Fig. 5C predicts that spike height after a temperature upshift will decrease with the activation energy of import. The activation energies of all other reactions were set to 15 kcal/mol (gray circle).

B) Increasing the activation energy of import to $E_a = 30\ \mathrm{kcal/mol}$ based on our experimental measurements of the activation energy of growth in glucose (Fig. S12G) dramatically reduced the spike height (green) compared with our default $E_a = 15\ \mathrm{kcal/mol}$ (red) without affecting the response time, similar to our experimental measurements of the normalized growth-rate response on glucose (green data, same as in Fig. 1H).

1113 C) The bottlenecked TSEN model predicts that short downshift pulses from 37 °C to
1114 27 °C (purple, red, orange) will cause larger spikes and faster recovery to the
1115 steady-state growth rate at 37 °C than an upshift from steady state at 27 °C to
1116 37 °C (blue), similar to our experimental observations (Fig. 1I).
1117 D,E) The bottlenecked TSEN model in Fig. 5C predicts that the response time
1118 decreases for downshift pulses of duration <1 doubling at the higher temperature
1119 (D) and that the spike height remains high for pulses of duration multiple
1120 doublings at the higher temperature (E).
1121 F,G,H) The bottlenecked TSEN model in Fig. 5C predicts that response time
1122 decreases (F), spike height increases (G), and growth activation energy
1123 decreases (H) when nutrient concentration is reduced from above (saturated, red
1124 circle) to below (unsaturated, purple circle) the K_M for import (gray vertical bar).
1125 I) Simulations of the bottlenecked TSEN model in Fig. 5C throughout an upshift
1126 from 27 °C to 37 °C for high (c_0=5 mM, red) or low (c_0=0.5 mM, purple) external
1127 substrate concentration ($K_M^{(import)}$ = 1 mM). The absolute spike height is similar in
1128 magnitude at both concentrations, but the steady-state growth rate at 37 °C is
1129 much lower for lower external substrate concentration (purple) and is reached
1130 more quickly after the upshift than for higher concentration (red).
1131 J) The normalized growth rate calculated from simulations in (H) has a larger spike
1132 and a faster normalized response (<1 doubling) for low external substrate
1133 concentration (purple) compared with the TSEN model at saturation (red).
1134 K,L) Growth rate throughout an upshift from 27 °C to 37 °C of *E. coli* MG1655 grown
1135 on MOPS+46 mM casamino acids (red, *n*=116 cells) or 4.6 mM casamino acids

1136 (purple, *n*=261 cells) exhibits similar dynamics in both absolute (J) and
1137 normalized (K) terms as the simulations in (H,I). Curves are mean growth rate
1138 and shaded regions represent ±1 SEM. The response time at low casamino acid
1139 concentration is much shorter (purple, ~0.25 doublings) compared to at
1140 saturation (red, ~1.4 doublings) and is accompanied by a larger relative spike
1141 height.

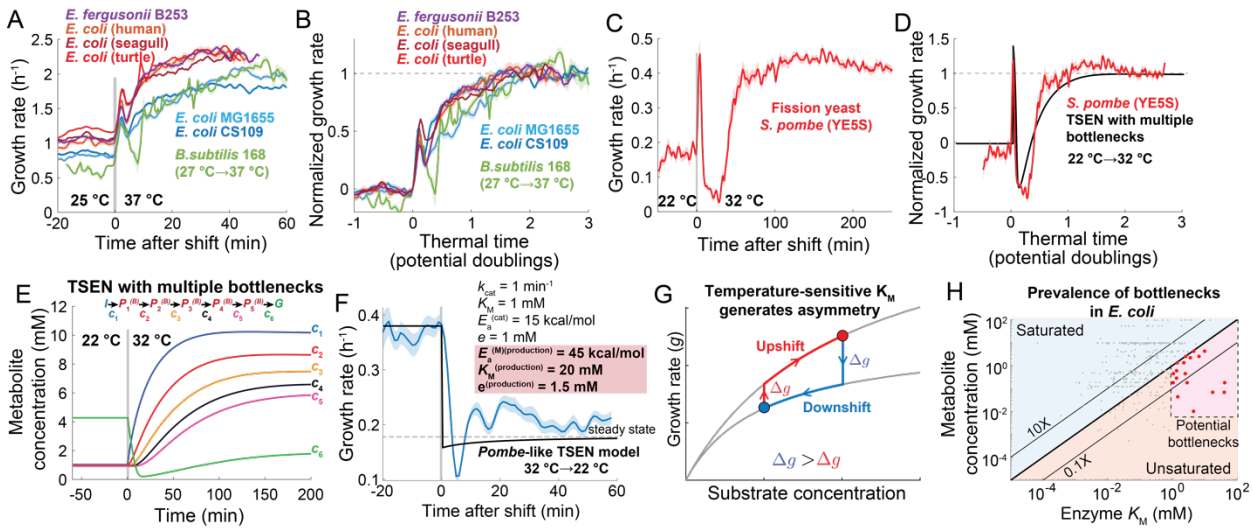

Figure 7: Temperature upshift response features are generally conserved across microbes and can be captured by the TSEN model.

A) Growth-rate response to a temperature upshift on LB of laboratory-evolved *E. coli* (light and dark blue, *n*=773–1279 cells) and natural isolates from various hosts (orange to red, *n*=389–547 cells), *Escherichia fergusonii* (purple, *n*=997 cells), and *Bacillus subtilis* (green, *n*=236 cells). All upshifts were from 25 °C to 37 °C, except for *B. subtilis* (27 °C to 37 °C). Curves are mean growth rate and shaded regions represent ±1 SEM.

B) Normalized growth rate followed a similar trajectory versus thermal time across all strains/species for the data in (A).

C) A temperature upshift from 22 °C to 32 °C on the rich growth medium YE5S caused the growth rate of the fission yeast *Schizosaccharomyces pombe* to initially spike to close to the steady-state value at 32 °C, then decelerate to below the steady-state value at 22 °C, then accelerate back to the new steady-state value within less than a doubling (~100 min) (red, *n*=333 cells). Curves are mean growth rate and shaded regions represent ±1 SEM.

1159 D) A TSEN model with 5 intermediate reactions, each with a large (20 mM) and
1160 highly temperature-sensitive K_M ($E_a^{(M)} = 22.5\ \mathrm{kcal/mol}$) produces similar
1161 normalized growth rate dynamics with thermal time (black) as the *S. pombe* data
1162 in (C) (red), characterized by a large spike, deceleration to <0, and fast recovery
1163 within <1 doubling.
1164 E) The TSEN model in (D), composed entirely of bottlenecks, predicts that a
1165 temperature upshift results in a rapid, large decrease in the final intermediate
1166 metabolite concentration (c_6), followed by a slower increase to the new steady-
1167 state, which is lower than at lower temperature. All other metabolite
1168 concentrations (c_{1-5}) increase monotonically toward their steady-state levels at
1169 rates that depend inversely on their network depth (i.e., c_5 increases more slowly
1170 than c_1).
1171 F) An extended TSEN model with five intermediate reactions, each with a large (20
1172 mM) and highly temperature-sensitive (E_a=22.5 kcal/mol) K_M, predicts a
1173 temporary undershoot (black) upon a downshift to growth rates below the steady
1174 state value at the lower temperature. The fission yeast *Schizosaccharomyces*
1175 *pombe* exhibited an undershoot during a downshift from 32 °C to 32 °C on rich
1176 medium (YE5S) (blue, *n*=54 cells) similar to model predictions. Experimental data
1177 are the mean±1 SEM (shaded region) at each time point.
1178 G) Asymmetry in growth-rate response to temperature up- and downshifts is caused
1179 by the temperature sensitivity of K_M. If substrate concentration is near the K_M and
1180 $E_a^{(M)} > 0$, an upshift causes a small initial increase in growth rate, followed by a
1181 slow increase in substrate concentration to the new K_M via production (red).

1182 Conversely, a downshift causes a comparatively larger initial decrease in growth
1183 rate, followed by a slow decrease in substrate concentration to the new K_M via
1184 dilution (blue).
1185 H) Intracellular metabolite concentrations are generally much higher than the K_M of
1186 their production enzyme for *E. coli* grown on glucose (data from Ref. [81]).
1187 However, some metabolites have concentrations near or below the K_M of their
1188 production, and potential bottlenecks (purple region, red points) are those with
1189 K_M>1 mM and substrate concentration $c<K_M$.

1190 **BIBLIOGRAPHY**

1191

1192 1. Kanjee, U., and Houry, W.A. (2013). Mechanisms of acid resistance in
1193 Escherichia coli. Annu Rev Microbiol *67*, 65-81. 10.1146/annurev-micro-092412-
1194 155708.
1195 2. Sleator, R.D., and Hill, C. (2002). Bacterial osmoadaptation: the role of osmolytes
1196 in bacterial stress and virulence. FEMS Microbiol Rev *26*, 49-71. 10.1111/j.1574-
1197 6976.2002.tb00598.x.
1198 3. Rojas, E., Theriot, J.A., and Huang, K.C. (2014). Response of Escherichia coli
1199 growth rate to osmotic shock. Proc Natl Acad Sci U S A *111*, 7807-7812.
1200 10.1073/pnas.1402591111.
1201 4. Dai, X., Zhu, M., Warren, M., Balakrishnan, R., Patsalo, V., Okano, H.,
1202 Williamson, J.R., Fredrick, K., Wang, Y.P., and Hwa, T. (2016). Reduction of
1203 translating ribosomes enables Escherichia coli to maintain elongation rates
1204 during slow growth. Nat Microbiol *2*, 16231. 10.1038/nmicrobiol.2016.231.
1205 5. Sunagawa, S., Coelho, L.P., Chaffron, S., Kultima, J.R., Labadie, K., Salazar, G.,
1206 Djahanschiri, B., Zeller, G., Mende, D.R., Alberti, A., et al. (2015). Ocean
1207 plankton. Structure and function of the global ocean microbiome. Science *348*,
1208 1261359. 10.1126/science.1261359.
1209 6. Melillo, J.M., Frey, S.D., DeAngelis, K.M., Werner, W.J., Bernard, M.J., Bowles,
1210 F.P., Pold, G., Knorr, M.A., and Grandy, A.S. (2017). Long-term pattern and
1211 magnitude of soil carbon feedback to the climate system in a warming world.
1212 Science *358*, 101-105. 10.1126/science.aan2874.

1213 7. Zhang, Y., and Gross, C.A. (2021). Cold Shock Response in Bacteria. Annu Rev
1214 Genet *55*, 377-400. 10.1146/annurev-genet-071819-031654.
1215 8. Richter, K., Haslbeck, M., and Buchner, J. (2010). The heat shock response: life
1216 on the verge of death. Mol Cell *40*, 253-266. 10.1016/j.molcel.2010.10.006.
1217 9. Barber, M.A. (1908). The Rate of Multiplication of Bacillus Coli at Different
1218 Temperatures. The Journal of Infectious Diseases *5*, 379-400.
1219 10.1093/infdis/5.4.379.
1220 10. Mohr, P.W., and Krawiec, S. (1980). Temperature characteristics and Arrhenius
1221 plots for nominal psychrophiles, mesophiles and thermophiles. J Gen Microbiol
1222 *121*, 311-317. 10.1099/00221287-121-2-311.
1223 11. Herendeen, S.L., VanBogelen, R.A., and Neidhardt, F.C. (1979). Levels of major
1224 proteins of Escherichia coli during growth at different temperatures. J Bacteriol
1225 *139*, 185-194. 10.1128/jb.139.1.185-194.1979.
1226 12. Knapp, B.D., and Huang, K.C. (2022). The Effects of Temperature on Cellular
1227 Physiology. Annu Rev Biophys *51*, 499-526. 10.1146/annurev-biophys-112221-
1228 074832.
1229 13. Chen, K., Gao, Y., Mih, N., O'Brien, E.J., Yang, L., and Palsson, B.O. (2017).
1230 Thermosensitivity of growth is determined by chaperone-mediated proteome
1231 reallocation. Proc Natl Acad Sci U S A *114*, 11548-11553.
1232 10.1073/pnas.1705524114.
1233 14. Phillips, R., Kondev, J., and Theriot, J. (2009). Physical Biology of the Cell
1234 (Garland Science).

1235 15. Hinshelwood, C.N. (1952). On the chemical kinetics of autosynthetic systems.
1236 Journal of the Chemical Society (Resumed), 745-755. 10.1039/JR9520000745.
1237 16. Iyer-Biswas, S., Wright, C.S., Henry, J.T., Lo, K., Burov, S., Lin, Y., Crooks, G.E.,
1238 Crosson, S., Dinner, A.R., and Scherer, N.F. (2014). Scaling laws governing
1239 stochastic growth and division of single bacterial cells. Proc Natl Acad Sci U S A
1240 *111*, 15912-15917. 10.1073/pnas.1403232111.
1241 17. Elias, M., Wieczorek, G., Rosenne, S., and Tawfik, D.S. (2014). The universality
1242 of enzymatic rate-temperature dependency. Trends Biochem Sci *39*, 1-7.
1243 10.1016/j.tibs.2013.11.001.
1244 18. Dill, K.A., Ghosh, K., and Schmit, J.D. (2011). Physical limits of cells and
1245 proteomes. Proc Natl Acad Sci U S A *108*, 17876-17882.
1246 10.1073/pnas.1114477108.
1247 19. Lemaux, P.G., Herendeen, S.L., Bloch, P.L., and Neidhardt, F.C. (1978).
1248 Transient rates of synthesis of individual polypeptides in E. coli following
1249 temperature shifts. Cell *13*, 427-434. 10.1016/0092-8674(78)90317-3.
1250 20. Gadgil, M., Kapur, V., and Hu, W.S. (2005). Transcriptional response of
1251 Escherichia coli to temperature shift. Biotechnol Prog *21*, 689-699.
1252 10.1021/bp049630l.
1253 21. Tagkopoulos, I., Liu, Y.C., and Tavazoie, S. (2008). Predictive behavior within
1254 microbial genetic networks. Science *320*, 1313-1317. 10.1126/science.1154456.
1255 22. Zhou, Y.N., Kusukawa, N., Erickson, J.W., Gross, C.A., and Yura, T. (1988).
1256 Isolation and characterization of Escherichia coli mutants that lack the heat shock

1257 sigma factor sigma 32. J Bacteriol *170*, 3640-3649. 10.1128/jb.170.8.3640-
1258 3649.1988.
1259 23. Chohji, T., Sawada, T., and Kuno, S. (1983). Effects of temperature shift on
1260 growth rate of Escherichia coli BB at lower glucose concentration. Biotechnol
1261 Bioeng *25*, 2991-3003. 10.1002/bit.260251215.
1262 24. Sinensky, M. (1974). Homeoviscous adaptation--a homeostatic process that
1263 regulates the viscosity of membrane lipids in Escherichia coli. Proc Natl Acad Sci
1264 U S A *71*, 522-525. 10.1073/pnas.71.2.522.
1265 25. Budin, I., de Rond, T., Chen, Y., Chan, L.J.G., Petzold, C.J., and Keasling, J.D.
1266 (2018). Viscous control of cellular respiration by membrane lipid composition.
1267 Science *362*, 1186-1189. 10.1126/science.aat7925.
1268 26. Scott, M., Klumpp, S., Mateescu, E.M., and Hwa, T. (2014). Emergence of robust
1269 growth laws from optimal regulation of ribosome synthesis. Mol Syst Biol *10*, 747.
1270 10.15252/msb.20145379.
1271 27. Bremer, H., and Dennis, P.P. (2008). Modulation of Chemical Composition and
1272 Other Parameters of the Cell at Different Exponential Growth Rates. EcoSal Plus
1273 *3*. 10.1128/ecosal.5.2.3.
1274 28. Belliveau, N.M., Chure, G., Hueschen, C.L., Garcia, H.G., Kondev, J., Fisher,
1275 D.S., Theriot, J.A., and Phillips, R. (2021). Fundamental limits on the rate of
1276 bacterial growth and their influence on proteomic composition. Cell Syst *12*, 924-
1277 944 e922. 10.1016/j.cels.2021.06.002.

1278 29. Zaritsky, A. (1982). Effects of growth temperature on ribosomes and other
1279 physiological properties of Escherichia coli. J Bacteriol *151*, 485-486.
1280 10.1128/jb.151.1.485-486.1982.
1281 30. Ram, J.L., Ritchie, R.P., Fang, J., Gonzales, F.S., and Selegean, J.P. (2004).
1282 Sequence-based source tracking of Escherichia coli based on genetic diversity of
1283 beta-glucuronidase. J Environ Qual *33*, 1024-1032. 10.2134/jeq2004.1024.
1284 31. Ram, J.L., Thompson, B., Turner, C., Nechvatal, J.M., Sheehan, H., and Bobrin,
1285 J. (2007). Identification of pets and raccoons as sources of bacterial
1286 contamination of urban storm sewers using a sequence-based bacterial source
1287 tracking method. Water Res *41*, 3605-3614. 10.1016/j.watres.2007.04.013.
1288 32. Knapp, B.D., Zhu, L., and Huang, K.C. (2020). SiCTeC: An inexpensive, easily
1289 assembled Peltier device for rapid temperature shifting during single-cell
1290 imaging. PLoS Biol *18*, e3000786. 10.1371/journal.pbio.3000786.
1291 33. Cashel, M., and Gallant, J. (1969). Two compounds implicated in the function of
1292 the RC gene of Escherichia coli. Nature *221*, 838-841. 10.1038/221838a0.
1293 34. Irving, S.E., Choudhury, N.R., and Corrigan, R.M. (2021). The stringent response
1294 and physiological roles of (pp)pGpp in bacteria. Nat Rev Microbiol *19*, 256-271.
1295 10.1038/s41579-020-00470-y.
1296 35. Mackow, E.R., and Chang, F.N. (1983). Correlation between RNA synthesis and
1297 ppGpp content in Escherichia coli during temperature shifts. Mol Gen Genet *192*,
1298 5-9. 10.1007/BF00327639.

1299 36. Scott, M., Gunderson, C.W., Mateescu, E.M., Zhang, Z., and Hwa, T. (2010).
1300 Interdependence of cell growth and gene expression: origins and consequences.
1301 Science *330*, 1099-1102. 10.1126/science.1192588.
1302 37. Maitra, A., and Dill, K.A. (2015). Bacterial growth laws reflect the evolutionary
1303 importance of energy efficiency. Proc Natl Acad Sci U S A *112*, 406-411.
1304 10.1073/pnas.1421138111.
1305 38. Reuveni, S., Ehrenberg, M., and Paulsson, J. (2017). Ribosomes are optimized
1306 for autocatalytic production. Nature *547*, 293-297. 10.1038/nature22998.
1307 39. Hui, S., Silverman, J.M., Chen, S.S., Erickson, D.W., Basan, M., Wang, J., Hwa,
1308 T., and Williamson, J.R. (2015). Quantitative proteomic analysis reveals a simple
1309 strategy of global resource allocation in bacteria. Mol Syst Biol *11*, 784.
1310 10.15252/msb.20145697.
1311 40. Schmidt, A., Kochanowski, K., Vedelaar, S., Ahrne, E., Volkmer, B., Callipo, L.,
1312 Knoops, K., Bauer, M., Aebersold, R., and Heinemann, M. (2016). The
1313 quantitative and condition-dependent Escherichia coli proteome. Nat Biotechnol
1314 *34*, 104-110. 10.1038/nbt.3418.
1315 41. Li, G.W., Burkhardt, D., Gross, C., and Weissman, J.S. (2014). Quantifying
1316 absolute protein synthesis rates reveals principles underlying allocation of
1317 cellular resources. Cell *157*, 624-635. 10.1016/j.cell.2014.02.033.
1318 42. Galperin, M.Y., Makarova, K.S., Wolf, Y.I., and Koonin, E.V. (2015). Expanded
1319 microbial genome coverage and improved protein family annotation in the COG
1320 database. Nucleic Acids Res *43*, D261-269. 10.1093/nar/gku1223.

1321 43. Grossberger, R., Mayer, O., Waldsich, C., Semrad, K., Urschitz, S., and
1322 Schroeder, R. (2005). Influence of RNA structural stability on the RNA chaperone
1323 activity of the Escherichia coli protein StpA. Nucleic Acids Res *33*, 2280-2289.
1324 10.1093/nar/gki515.
1325 44. Wetmore, K.M., Price, M.N., Waters, R.J., Lamson, J.S., He, J., Hoover, C.A.,
1326 Blow, M.J., Bristow, J., Butland, G., Arkin, A.P., and Deutschbauer, A. (2015).
1327 Rapid quantification of mutant fitness in diverse bacteria by sequencing randomly
1328 bar-coded transposons. mBio *6*, e00306-00315. 10.1128/mBio.00306-15.
1329 45. Murina, V., Kasari, M., Takada, H., Hinnu, M., Saha, C.K., Grimshaw, J.W., Seki,
1330 T., Reith, M., Putrins, M., Tenson, T., et al. (2019). ABCF ATPases Involved in
1331 Protein Synthesis, Ribosome Assembly and Antibiotic Resistance: Structural and
1332 Functional Diversification across the Tree of Life. J Mol Biol *431*, 3568-3590.
1333 10.1016/j.jmb.2018.12.013.
1334 46. Cochrane, K. (2015). Elucidating ribosomes—genetic studies of the ATPase Uup
1335 and the ribosomal protein L1. (University of Michigan).
1336 47. Sulavik, M.C., Houseweart, C., Cramer, C., Jiwani, N., Murgolo, N., Greene, J.,
1337 DiDomenico, B., Shaw, K.J., Miller, G.H., Hare, R., and Shimer, G. (2001).
1338 Antibiotic susceptibility profiles of Escherichia coli strains lacking multidrug efflux
1339 pump genes. Antimicrob Agents Chemother *45*, 1126-1136.
1340 10.1128/AAC.45.4.1126-1136.2001.
1341 48. Wilson, D.N. (2014). Ribosome-targeting antibiotics and mechanisms of bacterial
1342 resistance. Nat Rev Microbiol *12*, 35-48. 10.1038/nrmicro3155.

1343 49. Ikeuchi, Y., Shigi, N., Kato, J., Nishimura, A., and Suzuki, T. (2006). Mechanistic
1344 insights into sulfur relay by multiple sulfur mediators involved in thiouridine
1345 biosynthesis at tRNA wobble positions. Mol Cell *21*, 97-108.
1346 10.1016/j.molcel.2005.11.001.
1347 50. Campbell, J.W., and Cronan, J.E., Jr. (2001). Escherichia coli FadR positively
1348 regulates transcription of the fabB fatty acid biosynthetic gene. J Bacteriol *183*,
1349 5982-5990. 10.1128/JB.183.20.5982-5990.2001.
1350 51. Borgaro, J.G., Chang, A., Machutta, C.A., Zhang, X., and Tonge, P.J. (2011).
1351 Substrate recognition by beta-ketoacyl-ACP synthases. Biochemistry *50*, 10678-
1352 10686. 10.1021/bi201199x.
1353 52. Sorensen, T.H., Cruys-Bagger, N., Windahl, M.S., Badino, S.F., Borch, K., and
1354 Westh, P. (2015). Temperature Effects on Kinetic Parameters and Substrate
1355 Affinity of Cel7A Cellobiohydrolases. J Biol Chem *290*, 22193-22202.
1356 10.1074/jbc.M115.658930.
1357 53. Sizer, I.W. (1943). Effects of Temperature on Enzyme Kinetics. In Advances in
1358 Enzymology and Related Areas of Molecular Biology, pp. 35-62.
1359 https://doi.org/10.1002/9780470122488.ch2.
1360 54. Ehmann, J.D., and Hultin, H.O. (1973). Temperature dependence of the
1361 Michaelis constant of chicken breast muscle lactate dehydrogenase. Journal of
1362 Food Science *38*, 1119-1121. https://doi.org/10.1111/j.1365-
1363 2621.1973.tb07216.x.
1364 55. Monod, J. (1949). The Growth of Bacterial Cultures. Annual Review of
1365 Microbiology *3*, 371-394. 10.1146/annurev.mi.03.100149.002103.

1366 56. Garcia-Alles, L.F., Navdaeva, V., Haenni, S., and Erni, B. (2002). The glucose-
1367 specific carrier of the Escherichia coli phosphotransferase system. Eur J
1368 Biochem *269*, 4969-4980. 10.1046/j.1432-1033.2002.03197.x.
1369 57. Chang, A., Jeske, L., Ulbrich, S., Hofmann, J., Koblitz, J., Schomburg, I.,
1370 Neumann-Schaal, M., Jahn, D., and Schomburg, D. (2021). BRENDA, the
1371 ELIXIR core data resource in 2021: new developments and updates. Nucleic
1372 Acids Res *49*, D498-D508. 10.1093/nar/gkaa1025.
1373 58. Bao, H., Dalal, K., Cytrynbaum, E., and Duong, F. (2015). Sequential Action of
1374 MalE and Maltose Allows Coupling ATP Hydrolysis to Translocation in the
1375 MalFGK2 Transporter. J Biol Chem *290*, 25452-25460.
1376 10.1074/jbc.M115.671826.
1377 59. Bennett, B.D., Kimball, E.H., Gao, M., Osterhout, R., Van Dien, S.J., and
1378 Rabinowitz, J.D. (2009). Absolute metabolite concentrations and implied enzyme
1379 active site occupancy in Escherichia coli. Nat Chem Biol *5*, 593-599.
1380 10.1038/nchembio.186.
1381 60. Ritchie, M.E. (2018). Reaction and diffusion thermodynamics explain optimal
1382 temperatures of biochemical reactions. Sci Rep *8*, 11105. 10.1038/s41598-018-
1383 28833-9.
1384 61. Petersen, J., and Russell, P. (2016). Growth and the Environment of
1385 Schizosaccharomyces pombe. Cold Spring Harb Protoc *2016*, pdb top079764.
1386 10.1101/pdb.top079764.
1387 62. Neidhardt, F.C., and Curtiss, R. (1996). Escherichia coli and Salmonella : cellular
1388 and molecular biology, 2nd Edition (ASM Press).

1389 63. Atolia, E., Cesar, S., Arjes, H.A., Rajendram, M., Shi, H., Knapp, B.D., Khare, S.,
1390 Aranda-Diaz, A., Lenski, R.E., and Huang, K.C. (2020). Environmental and
1391 Physiological Factors Affecting High-Throughput Measurements of Bacterial
1392 Growth. mBio *11*. 10.1128/mBio.01378-20.
1393 64. Walk, S.T., Alm, E.W., Gordon, D.M., Ram, J.L., Toranzos, G.A., Tiedje, J.M.,
1394 and Whittam, T.S. (2009). Cryptic lineages of the genus Escherichia. Appl
1395 Environ Microbiol *75*, 6534-6544. 10.1128/AEM.01262-09.
1396 65. Reas, C., and Fry, B. (2006). Processing: programming for the media arts. AI &
1397 SOCIETY *20*, 526-538. 10.1007/s00146-006-0050-9.
1398 66. Edelstein, A., Amodaj, N., Hoover, K., Vale, R., and Stuurman, N. (2010).
1399 Computer control of microscopes using microManager. Curr Protoc Mol Biol
1400 *Chapter 14*, Unit14 20. 10.1002/0471142727.mb1420s92.
1401 67. Van Valen, D.A., Kudo, T., Lane, K.M., Macklin, D.N., Quach, N.T., DeFelice,
1402 M.M., Maayan, I., Tanouchi, Y., Ashley, E.A., and Covert, M.W. (2016). Deep
1403 Learning Automates the Quantitative Analysis of Individual Cells in Live-Cell
1404 Imaging Experiments. PLoS Comput Biol *12*, e1005177.
1405 10.1371/journal.pcbi.1005177.
1406 68. Tseng, Q., Wang, I., Duchemin-Pelletier, E., Azioune, A., Carpi, N., Gao, J.,
1407 Filhol, O., Piel, M., Thery, M., and Balland, M. (2011). A new micropatterning
1408 method of soft substrates reveals that different tumorigenic signals can promote
1409 or reduce cell contraction levels. Lab Chip *11*, 2231-2240. 10.1039/c0lc00641f.
1410 69. Schindelin, J., Arganda-Carreras, I., Frise, E., Kaynig, V., Longair, M., Pietzsch,
1411 T., Preibisch, S., Rueden, C., Saalfeld, S., Schmid, B., et al. (2012). Fiji: an open-

1412 source platform for biological-image analysis. Nat Methods *9*, 676-682.
1413 10.1038/nmeth.2019.
1414 70. Knapp, B.D., Odermatt, P., Rojas, E.R., Cheng, W., He, X., Huang, K.C., and
1415 Chang, F. (2019). Decoupling of Rates of Protein Synthesis from Cell Expansion
1416 Leads to Supergrowth. Cell Syst *9*, 434-445 e436. 10.1016/j.cels.2019.10.001.
1417 71. Ursell, T., Lee, T.K., Shiomi, D., Shi, H., Tropini, C., Monds, R.D., Colavin, A.,
1418 Billings, G., Bhaya-Grossman, I., Broxton, M., et al. (2017). Rapid, precise
1419 quantification of bacterial cellular dimensions across a genomic-scale knockout
1420 library. BMC Biol *15*, 17. 10.1186/s12915-017-0348-8.
1421 72. Traub, W.H., and Leonhard, B. (1995). Heat stability of the antimicrobial activity
1422 of sixty-two antibacterial agents. J Antimicrob Chemother *35*, 149-154.
1423 10.1093/jac/35.1.149.
1424 73. Shi, H., Hu, Y., Odermatt, P.D., Gonzalez, C.G., Zhang, L., Elias, J.E., Chang, F.,
1425 and Huang, K.C. (2021). Precise regulation of the relative rates of surface area
1426 and volume synthesis in bacterial cells growing in dynamic environments. Nat
1427 Commun *12*, 1975. 10.1038/s41467-021-22092-5.
1428 74. Karp, P.D., Paley, S., Caspi, R., Kothari, A., Krummenacker, M., Midford, P.E.,
1429 Moore, L.R., Subhraveti, P., Gama-Castro, S., Tierrafria, V.H., et al. (2023). The
1430 EcoCyc Database (2023). EcoSal Plus, eesp00022023.
1431 75. Axelrod, D., Koppel, D.E., Schlessinger, J., Elson, E., and Webb, W.W. (1976).
1432 Mobility measurement by analysis of fluorescence photobleaching recovery
1433 kinetics. Biophys J *16*, 1055-1069. 10.1016/S0006-3495(76)85755-4.
1434